J. Appl. Comput. Mech., 11(4) (2025) 1112-1138
DOI: 10.22055/jacm.2025.47828.4795

ISSN: 2383-4536
jacm.scu.ac.ir

Shahid Chamran University of Ahvaz

Journal of Applied and Computational Mechanics

Research Paper

The Effects of Defects and Adherend Material on Adhesive Stress Distribution in Laminated Composite Tubular Joints Under Axial Tensile Loads

M. Shishesaz, A.H. Ghamarian, R. Mosalmani

Mechanical Engineering Department, Faculty of Engineering, Shahid Chamran University of Ahvaz, Ahvaz, Iran,
Email: mshishehsaz@scu.ac.ir (M.S.); amhgh16@gmail.com (A.H.Gh.); mosalmani@scu.ac.ir (R.M.)

Received August 22 2024; Revised January 08 2025; Accepted for publication January 08 2025.
Corresponding author: M. Shishesaz (mshishehsaz@scu.ac.ir)

Abstract. This study focuses on the effects of an adhesive defect and adherend type and material on stress distribution in laminated composite tubular joints sustaining axial tensile loads. The tubular joint comprised two hollow tubes joined by a layer of adhesive to form a simple lap joint, hosting a cylindrical void or debond. The adherends were assumed to be either isotropic, quasi-isotropic, orthotropic, or transversely isotropic. Applying linear elasticity, the equilibrium equations were derived and solved using the differential quadrature method. Furthermore, finite element models of the joint were prepared and solved to support the semi-analytical solutions. Good agreements were observed between the results of both methods. Based on the results, for a defect-free joint with a bond length of 30 mm, nearly 80% of the bond length experienced zero peel stress (σ_r), while this value was about 20% for the peak interfacial shear stress $(\tau_{rx})_{\max}$. Additionally, among the selected types of glass/epoxy outer tubes, the $[0_8]$ lamination setup minimized $(\tau_{rx})_{\max}$ while $(\sigma_r)_{\max}$ was the least for the quasi-isotropic arrangement of $[0/90/-45/45]_S$. Moreover, replacing the aluminum inner tube with steel, reduced the tensile peak peel stress by 38% and increased the peak shear stresses by 12%. However, compared to a defect-free joint, a void/debond in the adhesive layer highly affected the magnitudes and locations of the adhesive peak interfacial shear and the tensile peel stresses. Additional results showed that in a defective adhesive hosting a void, the application of $[0_8]$ transversely isotropic carbon/epoxy can reduce the adhesive peak shear stresses by 200% compared to glass/epoxy.

Keywords: Tubular joint, adhesively bonded, stress distribution, composite tube.

1. Introduction

Adhesively bonded joints are used in a wide range of applications, from commercial to aerospace [1-5]. In this connection, the tubular joints are classified into two main types based on the shape of the bonded region: tubular lap joints and tubular socket joints. In single-lap tubular joints, the two adherends (or tubes) are joined by a layer of adhesive (see Fig. 1(a)). The adherends material can be isotropic, fiber-reinforced plastic, or any other composite type. In tubular socket joints, the two adherends (or tubes) are joined by a socket using a layer of adhesive (see Fig. 1(b)).

In these joints, the socket and/or pipe materials may be similar or different, which can affect the strength and durability of the joint. One of the main concerns in designing these joints is to minimize the maximum peel and shear stresses that occur in the adhesive layer. In the adhesively bonded joints, these stresses are a function of load, joint type, and the geometric and mechanical properties of the adhesive and the adherends. Depending on the load type and its magnitude, joint geometry, as well as physical and mechanical properties of the joint constituents, excessive stresses can develop in the adhesive layer causing its failure. For this purpose, many investigations have been conducted to estimate the stresses that develop in this layer and reduce their values to optimize the joint performance.

In the early studies by Goland and Reissner [6], stress distribution was investigated in cemented lap joints to establish a strong bond between plastic, wood, or metal sheets. The resulting solutions focused on two limiting cases. In case 1, the joint flexibility was ignored due to the thin layer of cement, and in case 2, the joint flexibility was mainly considered to be due to the adhesive layer. Later, in the study performed by Lubkin and Reissner [7], stress distributions in adhesively bonded circular tubes in tension were investigated. The adhesive behavior was assumed to be elastic and much more flexible than the adherends. The effect of various parameters on stress distribution was investigated. The inelastic behavior of the adhesive layer on adhesive stress distribution was investigated in [8]. Here, the Prony series was used to account for the viscoelastic behavior of the adhesive layer. Furthermore, the long-term redistribution of stresses in the adhesive layer was determined using the finite element method. In a different study, applying the finite element method, Adams and Peppiatt [9] investigated the adhesive stresses in axially and torsionally loaded tubular lap joints with isotropic adherends. Square-edged adhesive layer and adhesive with fillet were both considered in this analysis. The results were further compared against the closed-form solutions. Additionally, the effect of partial tapering of the adherends as well as the effect of adhesive fillet were investigated in this analysis.

In addition to [8], the effect of matrix inelastic behavior on shear stress in the adhesive layer of a single lap joint was investigated in [10]. In this analysis, the adhesive layer was assumed to have either a linear elastic or an inelastic behavior. According to the results, the inelastic behavior of the adhesive layer affects the stress distribution even at low levels of external loading. In Ref. [11], Stress distribution in adhesively bonded cylindrical lap joints with isotropic adherends was investigated. In this study, the adhesive layer was allowed to be flexible or inflexible. The approximate closed-form solutions for the shear and normal stress distributions were obtained using the concept of minimum complementary energy. Numerical examples were used to demonstrate the effects of different parameters on stress concentrations that occur near the joint ends. The influence of residual stresses on the strength of the tubular joints with isotropic adherends is discussed in [12]. In this reference, the static strength and load-bearing capacity of an adhesively bonded tubular joint subjected to axial load is discussed. It considers the effects of the nonlinear behavior of rubber-toughened epoxy and the residual thermal stresses in the adhesive that arise from the joint's fabrication on the stress distribution along the bond length of the resulting single lap joint. This joint was designed to bond two steel tubes. The finite element analysis and tensile tests were utilized to develop the failure model of the joint.

The investigation reported in [13] focuses on the optimal design of co-cured steel-composite single-lap tubular joints. The design parameters studied included the thickness ratio of the steel and composite substrates, the test temperature, the stacking sequence of the composite adherend, and the presence of a scarf in the steel substrate. The failure mode of the joint was analyzed by considering the nonlinear behavior of the steel adherend, as well as the failure modes of each substrate in the steel-composite joint. The stress analysis accounted for the nonlinearity in the behavior of steel adherend and the residual stresses resulting from the fabrication process of the composite substrate. However, the thermal characteristic of tubular joints under axial loads is covered in [14].

One of the major concerns in joint analysis is the adhesive behavior under both static and dynamic loads. The theoretical investigation presented in [15] uses a shear lag model to examine the dynamic response of a tubular single lap joint that contains a void and is subjected to a harmonic axial load. The analysis assumes that the adhesive layer exhibits viscoelastic behavior, while the 6061-T6 aluminum adherends are treated as linear elastic materials. The study discusses the effects of the material properties of both adherends and adhesive, as well as the geometric dimensions of the joint and the presence of the void, on the shear stress distribution in the joint and the system's first natural frequency. The findings indicate that when the void length is less than 40% of the overlap length, the presence of the defect has minimal impact on the system's response.

The study presented in [16] focuses on the failure load for brittle crack propagation, joint optimization, and crack detection based on the free vibration results of an adhesively bonded tubular joint subjected to axial load. The results indicate that, although the maximum shear stresses in the adhesive layer occur at the two end faces, the highest stress levels are found at the end of the stiffer tube. Notably, this stress does not reach zero, even in a joint with a theoretical bond length that is infinitely long. Additionally, a fracture energy criterion for both conventional and optimized joints was introduced to predict brittle crack propagation. The axial natural frequencies, which vary with crack length, were utilized for crack detection. Additional contributions to the stress distributions in the adhesive layer of a tubular joint via the application of variational method to the potential energy of deformation can be found in [17].

Adhesively bonded joints with glass-fiber reinforced polymeric adherends (pipes) are often used in areas that may be subjected to internal/external pressure and exposed to corrosive media. In such cases, the performance of these joints is of great importance. In this relation, the study performed in [18] considers the failure behavior of two small glass-fiber reinforced tubes bonded by an adhesive layer to a socket. The joint performance was tested with a high tensile load combined with two different internal pressures of zero and 32 bars. The analytical and experimental results showed that the initial damage more likely occurs when the joint is loaded with a high tensile load in the absence of internal pressure.

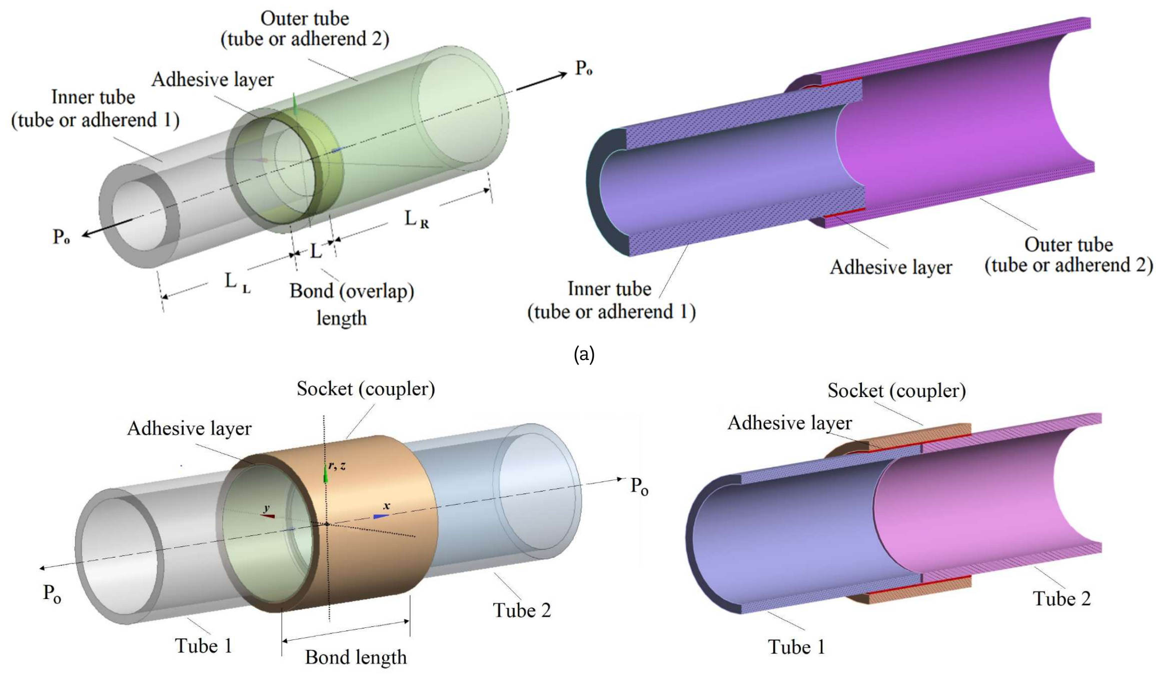

Fig. 1. Schematic diagrams of two adhesively bonded tubular joints, (a) A tubular adhesively bonded single-lap joint, (b) A tubular adhesively bonded socket joint.

One of the methods to increase the load-bearing capacity, strength, and lifetime of tubular joints is to reduce the stress concentrations occurring at the two ends of the overlap region. In this relation, the study performed in [19] has focused on the application of adhesives with a regulated modulus along the bond line. The study presents a theoretical framework that is based on the variational principle and is used to calculate the shear and peel stress distributions in a tubular joint under an axial force. According to the results, the peak shear and peel stresses are much smaller than those of a joint with a mono-modulus adhesive.

Using the finite element-based simulation technique, adhesion failure analysis of a tubular joint under a tensile external load and in the presence of a delaminated adherend was investigated in [20]. The adherends were composed of fiber-reinforced composite. Using the Tsai-Wu failure criterion, the effective overlap length required for proper joint performance was determined. Furthermore, using the virtual crack closure technique, the strain energy release rate was calculated to assess the adhesion failure. Results showed that adherends with plies oriented in the direction of the applied load show better resistance to in-plane shearing and opening mode growths of the adhesion failure. A parametric multi-objective optimization study on adhesively bonded tubular lap joints under an axial load was performed in [21]. Results showed that all geometric parameters affect the stress profile in the adhesive layer. The optimization study included six variables with three constraints and four objectives imposed on an axisymmetric two-dimensional finite element model. The study's objective included maximum normal and shear stresses, joint mass, and the equivalent stress in the adhesive layer.

In the study performed by Dragoni and Goglio [22], the underlying assumptions and accuracy of a few published results on the previous theoretical joint models under axial loads were reviewed. In a related study by Goglio and Paolino [23] on a tubular joint under axial load, using the Laplace transform, an explicit closed-form solution was obtained that was not reported in the Lubkin and Reissner model [7]. In this analysis, the adherends were treated as cylindrical thin shells subjected to bending and membrane stresses. Numerical examples were presented to support the formulations. Good results were obtained. In the study performed in [24] on tubular joints (with a socket or coupler, see Fig. 1(b)) under axial loads, a mathematical model was presented to calculate the distribution of stresses in the joint. Due to the joint geometric and loading, axisymmetric behavior was assigned to the joint. For the composite adherends, the effect of fiber angle forming the composite pipe was investigated. The effects of three different adhesives joining two tubular aluminum adherends under an axial load were studied in [25]. Finite element and experimental analyses were conducted to determine the distribution of peel and shear stresses in the adhesive layer. Furthermore, to predict the joint strength, cohesive zone models were employed to investigate the damage evolution.

In Refs. [26-27], the effect of a defect (in terms of a void or a debond) was studied *only on shear stress distribution* in the adhesive layer of a tubular single lap joint (see Fig. 1(a)) with *isotropic* adherends. The joint was either under torsion or an axial tensional load. Results indicated that the void's presence in the adhesive layer increases the peak shear stress near the overlap end for the joint in torsion. However, for a debond, the value and location of this stress depended on the length and location of the debond. For a near-edge debond, the peak shear stress occurred where the debond started. Similar behavior was observed for a tubular joint in tension.

Although there are a few other studies on tubular joints in tension, to the best of the authors' knowledge there is no experimental, analytical, or numerical work associated with the effect of adhesive defects on stress distribution in this layer for tubular joints in tension. In addition to the isotropic adherends, this study also focuses on the effects of material type and/or adherend's lamination setup (orthotropic, quasi-isotropic, or transversely isotropic) on the adhesive stresses, results of which are still missing in the literature. For this purpose, a novel mathematical approach is proposed that enables one to study the stress distributions in a defective adhesive hosting a cylindrical void or debond for a single lap tubular joint in tension. To achieve this, applying linear elasticity, the equilibrium equations are derived and solved using the differential quadrature method results of which are presented in Section 4. Additionally, finite element models are prepared and solved to back up the semi-analytical results. It is worth mentioning that the semi-analytical solution presented in this research, and similar works by other researchers, can effectively represent stress distribution in both brittle and ductile adhesive materials. Since polymeric adhesives have different properties, the terms "brittle" and "ductile" refer to the inherent characteristics of the specific polymer used in the analysis. For example, Araldite 2047-1 exhibits a ductile behavior while Araldite 2020 is brittle. As a consequence, the presented analysis can be applied to any type of adhesive used in joint analysis provided proper care is exercised in formulating and interpreting the results.

2. Derivation of Equilibrium Equations

Consider a cylindrical tubular single lap joint in tension as shown in Fig. 1(a). To derive the governing equilibrium equations, it is assumed that:

- Due to axisymmetric loading, the circumferential displacement in the adhesive layer can be assumed to be zero.
- The adherends and adhesive layer behave as linear elastic.
- The axial displacement function of the adhesive layer is of a second-order polynomial, expressed in the circumferential and axial directions. However, the function representing the adhesive radial displacement is assumed to be linear.
- According to the previous studies [26-27] and based on the coordinates shown in Fig. 2, the dominant stresses in the adhesive layer are the axial shear stress τ_{rx} and the peel stress σ_r.

Furthermore, to derive the equilibrium equation, the following strategy was applied [31]:

a) As the first step, the adhesive layer was assumed to be flawless. In this case, the governing equations of equilibrium were derived and used as the base equations, the results of which were used for further comparison. Based on this strategy, the governing elasticity equations were derived and solved to obtain the complete field equations.
b) In the second step, the adhesive layer was assumed to host either a cylindrical void or a cylindrical debond. Applying the proper boundary and continuity conditions in the adhesive layer, the deduced equilibrium equations were solved results of which were compared against those of a flawless adhesive (in step 1) to determine the effect of a defect on adhesive stresses.

2.1. Governing linear elasticity equations for a defect-free tubular single lap joint under a tensile load

Using the notations used in Fig. 2, the free-body diagrams of a portion of each tube were drawn as shown in Fig. 3. In this figure, the subscripts 1 and 2 refer to the inner and outer tubes (adherends), respectively. Moreover, to derive the equilibrium equations for the defect-free joint, τ_2 and τ_1 were allowed to be the shear stresses at the upper and lower adhesive-adherend interfaces (see Fig. 2) while σ was considered to be the peel stress.

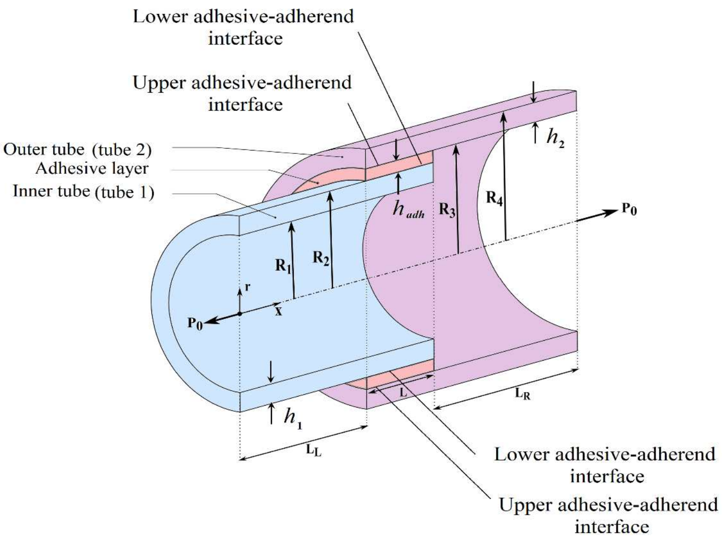

Fig. 2. Parameters and coordinate system used in [32].

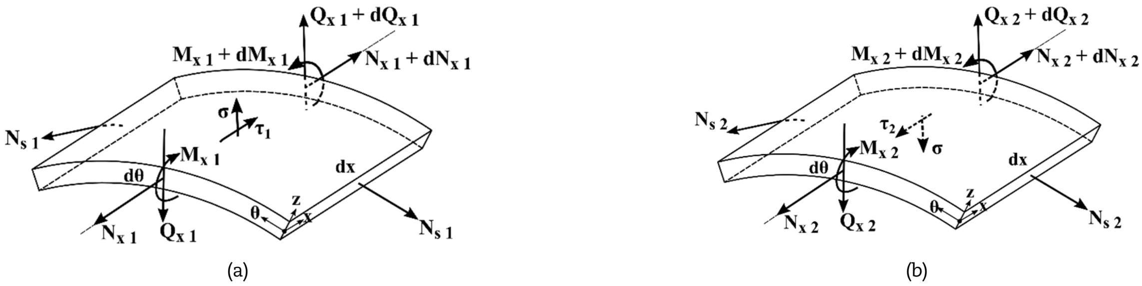

Fig. 3. The free-body diagrams of a differential element of each tube (adherends), (a) Inner tube (tube 1), (b) Outer tube (tube 2).

Considering $(Q_\theta)_m \equiv Q_m$, $(N_{x\theta})_m \equiv N_{xm}$, N_{sm}, $(M_{x\theta})_m \equiv M_{xm}$, and h_m (m = 1,2) as the transverse shear load/unit length, the resultant axial load /unit length, the circumferential load /unit length, the bending moment/unit length, and each tube thickness, respectively, application of the force equilibrium equations on a differential element of each tube in the axial direction gives:

$$\frac{dN_{x\,1}}{dx} = -\tau_1 \frac{R_2}{\bar{R}_1} \tag{1a}$$

$$\frac{dN_{x\,2}}{dx} = \tau_2 \frac{R_3}{\bar{R}_2} \tag{1b}$$

In Eqs. (1a) and (1b), $\bar{R}_1$ and $\bar{R}_2$ are defined as:

$$\bar{R}_1 = \frac{R_1 + R_2}{2} \tag{2}$$

$$\bar{R}_2 = \frac{R_3 + R_4}{2} \tag{3}$$

where R_i (i = 1-4) are the inner and outer radii of tubes 1 and 2, respectively (see Fig. 2).

Moreover, the application of bending moment along an edge line of the differential tube element perpendicular to the x-axis gives:

$$\frac{dM_{x\,1}}{dx} = Q_{x\,1} - \tau_1 \frac{R_2}{\bar{R}_1}\frac{h_1}{2} \tag{4a}$$

$$\frac{dM_{x\,2}}{dx} = Q_{x\,2} - \tau_2 \frac{R_3}{\bar{R}_2}\frac{h_2}{2} \tag{4b}$$

On the other hand, equilibrium equations (5a) and (5b) are obtained by applying the force-equilibrium equations in the radial direction "r" as:

$$\frac{dQ_{x\,1}}{dx} - \frac{N_{s\,1}}{\bar{R}_1} = -\frac{R_2}{\bar{R}_1}\sigma \tag{5a}$$

$$\frac{dQ_{x\,2}}{dx}-\frac{N_{s\,2}}{\bar{R}_2}=\frac{R_3}{\bar{R}_2}\sigma \tag{5b}$$

Additionally, for the portion of each tube (adherend) outside the bond length (with the lengths L_L and L_R, see Fig. 2), the pertinent equilibrium equations distinguished by the superscript "*bp*" are:

$$\frac{dN_{x\,1}^{(bp)}}{dx}=0 \tag{6a}$$

$$\frac{dN_{x\,2}^{(bp)}}{dx}=0 \tag{6b}$$

$$\frac{dM_{x\,1}^{(bp)}}{dx}=Q_{x\,1}^{(bp)} \tag{7a}$$

$$\frac{dM_{x\,2}^{(bp)}}{dx}=Q_{x\,2}^{(bp)} \tag{7b}$$

$$\frac{dQ_{x\,1}^{(bp)}}{dx}-\frac{N_{s\,1}^{(bp)}}{\bar{R}_1}=0 \tag{8a}$$

$$\frac{dQ_{x\,1}^{(bp)}}{dx}-\frac{N_{s\,1}^{(bp)}}{\bar{R}_1}=0 \tag{8b}$$

According to Fig. 4, the equilibrium of forces on either portion of the joint assembly (in this case left portion) requires that:

$$P_1(x)+P_2(x)+P_{adh}(x)=P_0 \tag{9}$$

In Eq. (9), $P_{adh}(x)$ is the tensional load in the adhesive, while $P_1(x)$ and $P_1(x)$ are similar loads in adherends 1 and 2, respectively.

Since each tube is under axisymmetric loading, the axial and radial displacement components of the displacements, namely, $u_i(x,z)$ and $w_i(x)$, are independent of the circumferential direction θ. Hence based on the previous assumptions we can write:

$$u_i(x,z)=u_{0\,i}(x)+z\kappa_{x\,i}(x) \tag{10}$$

$$w_i(x)=w_{0\,i}(x) \tag{11}$$

In Eqs. (10) and (11), parameter z which is measured along the radial direction "*r*' is the local distance between any point along each tube thickness and its mid-plane surface. Moreover, $w_{0\,i}(x)$, $\kappa_{x\,i}(x)$, and $u_{0\,i}(x)$, are the tube radial displacement, curvature, and mid-plane axial displacement functions, respectively. Applying linear elasticity equations while using Eqs. (10) and (11), the strain components are obtained in terms of curvatures and displacements (and/or their derivatives). Assuming either an orthotropic, quasi-isotropic, transversely isotropic, or isotropic behavior for the adherend materials, the stress-strain relations can be written as:

$$\sigma=\bar{\mathbf{Q}}\,\varepsilon \tag{12a}$$

where $\bar{\mathbf{Q}}$ is the 6×6 reduced stiffness matrix, ε is the 6×1 strain vector, and σ is the 6×1 stress vector with the following general components:

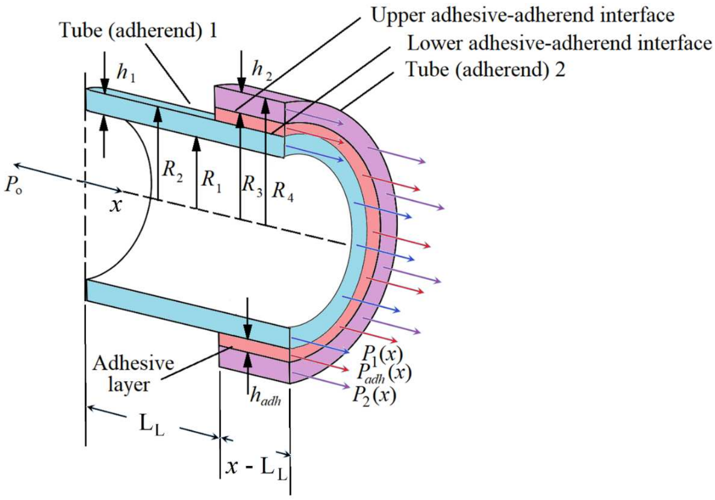

Fig. 4. Force balance on a cut portion of the tubular joint (dimensions not to scale).

$$\{\tilde{\sigma}\} = \{\sigma_x \quad \sigma_\theta \quad \sigma_r \quad \tau_{r\theta} \quad \tau_{rx} \quad \tau_{x\theta}\}^T \tag{12b}$$

$$\{\tilde{\varepsilon}\} = \{\varepsilon_x \quad \varepsilon_\theta \quad \varepsilon_r \quad \gamma_{r\theta} \quad \gamma_{rx} \quad \gamma_{x\theta}\}^T \tag{12c}$$

$$[\bar{Q}] = \begin{bmatrix} \bar{Q}_{11} & \bar{Q}_{12} & \bar{Q}_{13} & 0 & 0 & \bar{Q}_{16} \\ \bar{Q}_{12} & \bar{Q}_{22} & \bar{Q}_{23} & 0 & 0 & \bar{Q}_{26} \\ \bar{Q}_{13} & \bar{Q}_{23} & \bar{Q}_{33} & 0 & 0 & \bar{Q}_{36} \\ 0 & 0 & 0 & \bar{Q}_{44} & \bar{Q}_{45} & 0 \\ 0 & 0 & 0 & \bar{Q}_{45} & \bar{Q}_{55} & 0 \\ \bar{Q}_{16} & \bar{Q}_{26} & \bar{Q}_{36} & 0 & 0 & \bar{Q}_{66} \end{bmatrix} \tag{12d}$$

Using the coordinate system shown in Fig. 2, based on Eqs. (10) and (11), as well as the forgoing assumptions, the strain components are written in terms of displacement components as:

$$\varepsilon_{r\,i} = \gamma_{r\theta\,i} = \gamma_{x\theta\,i} = 0 \qquad (i = 1, 2) \tag{13a}$$

$$\varepsilon_{x\,i} = \frac{du_{0\,i}(x)}{dx} + z\frac{d\kappa_{x\,i}(x)}{dx} \tag{13b}$$

$$\varepsilon_{\theta\,i} = \frac{w_{0\,i}(x)}{R_i + z} \tag{13c}$$

$$\gamma_{rx\,i} = \kappa_{x\,i}(x) + \frac{dw_{0\,i}(x)}{dx} \tag{13d}$$

One using the expressions (12a-12c) as well as the strain displacement equations, the resulting stress components in each adherend layer is (i = 1, 2):

$$\sigma_{x\,i}^{(k)} = \bar{Q}_{11}^{(k)}\left[\frac{du_{0\,i}(x)}{dx} + z\frac{d\kappa_{x\,i}(x)}{dx}\right] + \bar{Q}_{12}^{(k)}\frac{w_{0\,i}(x)}{R_i + z} \tag{14a}$$

$$\sigma_{\theta\,i}^{(k)} = \bar{Q}_{12}^{(k)}\left[\frac{du_{0\,i}(x)}{dx} + z\frac{d\kappa_{x\,i}(x)}{dx}\right] + \bar{Q}_{22}^{(k)}\frac{w_{0\,i}(x)}{R_i + z} \tag{14b}$$

$$\sigma_{r\,i}^{(k)} = \bar{Q}_{13}^{(k)}\left[\frac{du_{0\,i}(x)}{dx} + z\frac{d\kappa_{x\,i}(x)}{dx}\right] + \bar{Q}_{23}^{(k)}\frac{w_{0\,i}(x)}{R_i + z} \tag{14c}$$

$$\tau_{r\theta\,i}^{(k)} = \bar{Q}_{45}^{(k)}\left[\kappa_{x\,i}(x) + \frac{dw_{0\,i}(x)}{dx}\right] \tag{14d}$$

$$\tau_{rx\,i}^{(k)} = \bar{Q}_{55}^{(k)}\left[\kappa_{x\,i}(x) + \frac{dw_{0\,i}(x)}{dx}\right] \tag{14e}$$

$$\tau_{x\theta\,i}^{(k)} = \bar{Q}_{16}^{(k)}\left[\frac{du_{0\,i}(x)}{dx} + z\frac{d\kappa_{x\,i}(x)}{dx}\right] + \bar{Q}_{16}^{(k)}\frac{w_{0\,i}(x)}{R_i + z} \tag{14f}$$

Furthermore, the expressions for loads and moments/unit length can be calculated according to the following equations:

$$\begin{Bmatrix} N_x \\ N_\theta \\ N_{x\theta} \\ N_{\theta x} \end{Bmatrix} = \sum_{k=1}^{n}\int_{z_k}^{z_{k+1}} \begin{Bmatrix} \sigma_x^{(k)}(1+\frac{z}{R}) \\ \sigma_\theta^{(k)} \\ \tau_{x\theta}^{(k)}(1+\frac{z}{R}) \\ \tau_{x\theta}^{(k)} \end{Bmatrix} dz, \quad \begin{Bmatrix} M_x \\ M_\theta \\ M_{x\theta} \\ M_{\theta x} \end{Bmatrix} = \sum_{k=1}^{n}\int_{z_k}^{z_{k+1}} \begin{Bmatrix} \sigma_x^{(k)}(1+\frac{z}{R}) \\ \sigma_\theta^{(k)} \\ \tau_{x\theta}^{(k)}(1+\frac{z}{R}) \\ \tau_{x\theta}^{(k)} \end{Bmatrix} zdz, \tag{15a}$$

$$\begin{Bmatrix} Q_x \\ Q_\theta \end{Bmatrix} = K_S\sum_{k=1}^{n}\int_{z_k}^{z_{k+1}} \begin{Bmatrix} \tau_{rx}^{(k)}(1+\frac{z}{R}) \\ \tau_{r\theta}^{(k)} \end{Bmatrix} dz \tag{15b}$$

In Eq. (15b), K_S is the shear correction factor and is considered to be 5/6 [32]. On using Eqs. (14a)-(14f), the expressions for variation of the loads and moments/unit length in each tube (i = 1, 2) are determined as:

$$N_{x\,i} = \left(A_{11}^{(i)} + \frac{1}{\bar{R}_i}B_{11}^{(i)}\right)\frac{du_{0\,i}(x)}{dx} + \left(B_{11}^{(i)} + \frac{1}{\bar{R}_i}D_{11}^{(i)}\right)\frac{d\kappa_{x\,i}(x)}{dx} + \frac{A_{12}^{(i)}}{\bar{R}_i}w_{0\,i}(x) \tag{16}$$

$$N_{s\,i} = A_{12}^{(i)}\frac{du_{0\,i}(x)}{dx} + B_{12}^{(i)}\frac{d\kappa_{x\,i}(x)}{dx} + F_{22}^{(i)}w_{0\,i}(x) \tag{17}$$

$$Q_{x\,i} = K_S\left(A_{55}^{(i)} + \frac{1}{\bar{R}_i}B_{55}^{(i)}\right)\kappa_{x\,i}(x) + K_S\left(A_{55}^{(i)} + \frac{1}{\bar{R}_i}B_{55}^{(i)}\right)\frac{dw_{0\,i}(x)}{dx} \tag{18}$$

$$M_{x\,i} = \left(B_{11}^{(i)} + \frac{1}{\bar{R}_i}D_{11}^{(i)}\right)\frac{du_{0\,i}(x)}{dx} + \left(D_{11}^{(i)} + \frac{1}{\bar{R}_i}E_{11}^{(i)}\right)\frac{d\kappa_{x\,i}(x)}{dx} + \frac{B_{12}^{(i)}}{\bar{R}_i}w_{0\,i}(x) \tag{19}$$

However, the D_{ij} elements of the bending stiffness matrix **D**, B_{ij} elements of the coupling matrix **B**, A_{ij} elements of the extensional stiffness matrix **A**, E_{ij} and F_{ij} elements of the two additional matrices **E** and **F** are defined and obtained according to the following equations:

$$A_{ij} = \int_{\frac{-h}{2}}^{\frac{h}{2}}\bar{Q}_{ij}dz = \sum_{k=1}^{N}\bar{Q}_{ij}^{(k)}\left(z_{k+1} - z_k\right) \tag{20a}$$

$$B_{ij} = \int_{\frac{-h}{2}}^{\frac{h}{2}}\bar{Q}_{ij}z\,dz = \frac{1}{2}\sum_{k=1}^{N}\bar{Q}_{ij}^{(k)}\left(z^2{}_{k+1} - z^2{}_k\right) \tag{20b}$$

$$D_{ij} = \int_{\frac{-h}{2}}^{\frac{h}{2}}\bar{Q}_{ij}z^2dz = \frac{1}{3}\sum_{k=1}^{N}\bar{Q}_{ij}^{(k)}\left(z^3{}_{k+1} - z^3{}_k\right) \tag{20c}$$

$$E_{ij} = \int_{\frac{-h}{2}}^{\frac{h}{2}}\bar{Q}_{ij}z^3dz = \frac{1}{4}\sum_{k=1}^{N}\bar{Q}_{ij}^{(k)}\left(z^4{}_{k+1} - z^4{}_k\right) \tag{20d}$$

$$F_{ij} = \int_{\frac{-h}{2}}^{\frac{h}{2}}\frac{\bar{Q}_{ij}}{\bar{R}+z}dz = \sum_{k=1}^{N}\bar{Q}_{ij}^{(k)}\ln\left(\frac{\bar{R}+z_{k+1}}{\bar{R}+z_k}\right) \tag{20e}$$

In these equations, h is each tube wall thickness and N refers to the total number of layers used to fabricate the composite adherends. For the isotropic adherend $N = 1$. Moreover, subscript k is used to number the layers in composite adherends.

Furthermore, a quadratic function was assumed for the axial displacement in the adhesive layer to allow for the variation of shear stress in its thickness direction. The pertinent expression is presented as:

$$u_{adh}(x,r) = \eta_0(r)u_0(x) + \eta_1(r)u_1(x) + \eta_2(r)u_2(x) \tag{21}$$

Here, the three functions $\eta_2(r)$, $\eta_1(r)$, and $\eta_0(r)$, are obtained using the following boundary conditions:

$$u_{adh}(x, r = \bar{R}_{adh}) = u_0(x)\ ,\ \bar{R}_{adh} = \frac{R_2 + R_3}{2} \tag{22a}$$

$$u_{adh}(x, r = R_2) = u_1(x) \tag{22b}$$

$$u_{adh}(x, r = R_3) = u_2(x) \tag{22c}$$

where the two functions $u_2(x)$, $u_1(x)$ are the adhesive axial displacements at its upper and lower surfaces, and $u_0(x)$ is the axial displacement at its mid-plane, respectively. The two functions $u_2(x)$, and $u_1(x)$ are determined in terms of other functions as:

$$u_2(x) = U_2(x, z = -\frac{h_2}{2}) = u_{0\,2}(x) - \frac{h_2}{2}\kappa_{x\,2}(x) \tag{23a}$$

$$u_1(x) = u_1(x, z = \frac{h_1}{2}) = u_{0\,1}(x) + \frac{h_1}{2}\kappa_{x\,1}(x) \tag{23b}$$

In Eqs. (23a) and (23b), $u_{0\,2}(x)$ and $u_{0\,1}(x)$ correspond to the adherends 1 and 2 mid-plane axial displacements. Now, the radial displacement in the adhesive layer is expressed as:

$$w_{adh}(x,r) = \omega_1(r)w_{0\,1}(x) + \omega_2(r)w_{0\,2}(x) \tag{24}$$

where the two functions $\omega_1(r)$ and $\omega_2(r)$ are defined according to the following boundary conditions:

$$w_{adh}(x, r = R_2) = w_{01}(x) \tag{25a}$$

$$w_{adh}(x,r=R_3)=w_{02}(x) \tag{25b}$$

Using the expressions for strain-displacements in the adhesive layer and substituting the results back into the expressions for stresses, one can show that the axial and normal stresses in the adhesive layer, $\sigma_{x\ adh}(x,r)$ and $\sigma_{r\ adh}(x)$, as well as the shear stress component $\tau_{rx\ adh}(x,r)$, can be expressed in terms of displacement components (or their derivatives) as:

$$\sigma_{x\ adh}(x,r)=E_{adh}\left[\eta_0(r)\frac{du_0(x)}{dx}+\eta_1(r)\frac{du_1(x)}{dx}+\eta_2(r)\frac{du_2(x)}{dx}\right] \tag{26a}$$

$$\sigma_{r\ adh}(x)=E_{adh}\frac{w_{02}(x)-w_{01}(x)}{R_3-R_2} \tag{26b}$$

$$\tau_{rx\ adh}(x,r)=G_{adh}\left[\frac{d\eta_0(r)}{dr}u_0(x)+\frac{d\eta_1(r)}{dr}u_1(x)+\frac{d\eta_2(r)}{dr}u_2(x)\right]+G_{adh}\left[\omega_1(r)\frac{dw_{0\ 1}(x)}{dx}+\omega_2(r)\frac{dw_{0\ 2}(x)}{dx}\right] \tag{26c}$$

In Eqs. (26a)-(26c), E_{adh} and G_{adh} are the elastic and shear moduli of the isotropic adhesive, respectively. Now, the shear stress components τ_1 and τ_2 at the lower and upper adhesive-adherend interfaces are defined as:

$$\tau_1=\tau_{rx,adh}(x,r=R_2) \tag{27a}$$

$$\tau_2=\tau_{rx,adh}(x,r=R_3) \tag{27b}$$

Moreover, the function presenting the axial load in the adhesive layer is:

$$P_{adh}(x)=2\pi\int_{R_2}^{R_3}r\sigma_{x\ adh}(x,r)dr \tag{28a}$$

$$P_{adh}(x)=2\pi E_{adh}\int_{R_2}^{R_3}\left[\eta_0(r)\frac{du_0(x)}{dx}+\eta_1(r)\frac{du_1(x)}{dx}+\eta_2(r)\frac{du_2(x)}{dx}\right]rdr \tag{28b}$$

Now, for simplicity, the three functions $\xi_1,\xi_2,$ and ξ_3 are defined as follows:

$$\xi_i=2\pi E_{adh}\int_{R_2}^{R_3}r\eta_{(i-1)}(r)dr \qquad (i = 1, 2, 3) \tag{29}$$

Based on these definitions, upon integration of Eq. (28b), the axial load in the adhesive layer is recast in the following form:

$$P_{adh}(x)=\xi_1\frac{du_0(x)}{dx}+\xi_2\left(\frac{du_{0\ 1}(x)}{dx}+\frac{h_1}{2}\frac{d\kappa_{x\ 1}(x)}{dx}\right)+\xi_3\left(\frac{du_{0\ 2}(x)}{dx}-\frac{h_2}{2}\frac{d\kappa_{x\ 2}(x)}{dx}\right) \tag{30}$$

where h_1 and h_2 are the thicknesses of the two tubes 1 and 2, respectively. Since:

$$P_i(x)=2\pi\bar{R}_iN_{xi}(x), \qquad (i = 1, 2) \tag{31}$$

then, the axial load distributions in tubes 1 and 2 can be expressed in terms of the A_{ij}, B_{ij}, and D_{ij} elements of each tube as:

$$P_i(x)=2\pi\bar{R}_i\left[\left(A_{11}^{(i)}+\frac{1}{\bar{R}_i}B_{11}^{(i)}\right)\frac{du_{0i}(x)}{dx}+\left(B_{11}^{(i)}+\frac{1}{\bar{R}_i}D_{11}^{(i)}\right)\frac{d\kappa_{xi}(x)}{dx}+\frac{A_{12}^{(i)}}{\bar{R}_i}w_{0i}(x)\right], \qquad (i =1, 2) \tag{32}$$

The superscripts (1) and (2) on the above parameters refer to the properties related to tubes 1 and 2 respectively.

On application of Eqs. (16)-(19), (26b)-(26c), (30), and (31) into equilibrium equations (1) to (8), the following coupled differential equations were obtained, solution of which were determined using differential quadrature method. These solutions were used to determine the stress distributions τ_1, τ_2, and σ_r in the adhesive layer along the bond length:

$$J_1\frac{d^2u_{0\ 1}(x)}{dx^2}+J_2\frac{d^2\kappa_{x\ 1}(x)}{dx^2}+J_3\frac{dw_{01}(x)}{dx}+J_4\frac{du_{0\ 1}(x)}{dx}+J_5\frac{d\kappa_{x\ 1}(x)}{dx}+J_6\frac{du_{0\ 2}(x)}{dx}+J_7\frac{d\kappa_{x\ 2}(x)}{dx}+J_8\frac{du_0(x)}{dx}=0 \tag{33a}$$

$$J_9\frac{d^2u_{0\ 2}(x)}{dx^2}+J_{10}\frac{d^2\kappa_{x\ 2}(x)}{dx^2}+J_{11}\frac{dw_{02}(x)}{dx}+J_{12}\frac{du_{0\ 1}(x)}{dx}+J_{13}\frac{d\kappa_{x\ 1}(x)}{dx}+J_{14}\frac{du_{0\ 2}(x)}{dx}+J_{15}\frac{d\kappa_{x\ 2}(x)}{dx}+J_{16}\frac{du_0(x)}{dx}=0 \tag{33b}$$

$$J_2\frac{d^2u_{0\ 1}(x)}{dx^2}+J_{17}\frac{d^2\kappa_{x\ 1}(x)}{dx^2}+J_{18}\frac{dw_{0\ 2}(x)}{dx}+J_{19}\frac{du_{0\ 1}(x)}{dx}+J_{20}\frac{d\kappa_{x\ 1}(x)}{dx}+J_{21}\frac{du_{0\ 2}(x)}{dx}+J_{22}\frac{d\kappa_{x\ 2}(x)}{dx}+J_{23}\frac{du_0(x)}{dx}=0 \tag{33c}$$

$$J_{10}\frac{d^2u_{0\ 2}(x)}{dx^2}+J_{24}\frac{d^2\kappa_{x\ 2}(x)}{dx^2}+J_{25}\frac{dw_{0\ 2}(x)}{dx}+J_{26}\frac{du_{0\ 1}(x)}{dx}+J_{27}\frac{d\kappa_{x\ 1}(x)}{dx}+J_{28}\frac{du_{0\ 2}(x)}{dx}+J_{29}\frac{d\kappa_{x\ 2}(x)}{dx}+J_{30}\frac{du_0(x)}{dx}=0 \tag{33d}$$

$$J_{31}\frac{du_{0\ 1}(x)}{dx}+J_{32}\frac{d\kappa_{x\ 1}(x)}{dx}+J_{33}\frac{d^2w_{0\ 2}(x)}{dx^2}+J_{34}\frac{dw_{0\ 1}}{dx}+J_{35}\frac{dw_{0\ 2}}{dx}=0 \tag{33e}$$

$$J_{36}\frac{du_{0\,2}(x)}{dx}+J_{37}\frac{d\kappa_{x\,2}(x)}{dx}+J_{38}\frac{d^2w_{0\,2}(x)}{dx^2}+J_{39}\frac{dw_{0\,1}}{dx}+J_{40}\frac{dw_{0\,2}}{dx}=0 \tag{33f}$$

$$J_{41}\frac{du_{0\,1}(x)}{dx}+J_{42}\frac{d\kappa_{x\,1}(x)}{dx}+J_{43}w_{0\,1}(x)+J_{44}\frac{du_{0\,2}(x)}{dx}+J_{45}\frac{d\kappa_{x\,2}(x)}{dx}+J_{46}w_{0\,2}(x)+J_{47}\frac{du_0(x)}{dx}=0 \tag{33g}$$

$$J_1\frac{d^2u_{0\,1}(x)}{dx^2}+J_2\frac{d^2\kappa_{x\,1}(x)}{dx^2}+J_{48}w_{0\,1}(x)=0 \tag{33h}$$

$$J_9\frac{d^2u_{0\,2}(x)}{dx^2}+J_{10}\frac{d^2\kappa_{x\,2}(x)}{dx^2}+J_{49}w_{0\,2}(x)=0 \tag{33i}$$

$$J_2\frac{d^2u_{0\,1}(x)}{dx^2}+J_{17}\frac{d^2\kappa_{x\,1}(x)}{dx^2}+J_{50}\frac{dw_{0\,1}(x)}{dx}+J_{51}\kappa_{x\,1}(x)=0 \tag{33j}$$

$$J_{10}\frac{d^2u_{0\,2}(x)}{dx^2}+J_{24}\frac{d^2\kappa_{x\,2}(x)}{dx^2}+J_{52}\frac{dw_{0\,2}(x)}{dx}+J_{53}\kappa_{x\,2}(x)=0 \tag{33k}$$

$$J_{51}\frac{d^2w_{0\,1}(x)}{dx^2}+J_{54}\frac{du_{0\,1}(x)}{dx}+J_{55}\frac{d\kappa_{x\,1}(x)}{dx}+J_{56}w_{0\,1}(x)=0 \tag{33l}$$

The coefficients J_1-J_{56} are given in terms of other parameters in Appendix A. To fully define the field equations and solve the previous differential equations, 25 boundary and continuity conditions were necessary. With the help of Eq. (9) and the geometric conditions of the joint shown in Figs. 2 and 4, the corresponding relations were deduced as introduced in Eqs. (34)-(37) [32].

- At $x = 0$;

$$N_{x\,1}^{(bp)}(0)=\frac{P_0}{2\pi\bar{R}_1}\quad,\quad M_{x\,1}^{(bp)}(0)=0\quad,\quad Q_{x\,1}^{(bp)}(0)=0 \tag{34}$$

(Application of axial load/length, zero bending moment/length, and zero transverse shear load/length at the left face of the inner tube, see Fig. 2)

- At $x = L_L$;

$$N_{x\,2}(L_L)=0\quad,\quad M_{x\,2}(L_L)=0\quad,\quad Q_{x\,2}(L_L)=0 \tag{35a}$$

(Application of zero axial load/length, zero bending moment/length, and zero transverse shear load/length at the left face (free edge) of the outer tube, see Fig. 2)

$$u_{0\,1}^{(bp)}(L_L)=u_{0\,1}(L_L)\quad,\quad \left.\frac{du_{0\,1}^{(bp)}(x)}{dx}\right|_{x=L_L}=\left.\frac{du_{0\,1}(x)}{dx}\right|_{x=L_L} \tag{35b}$$

$$\kappa_{x\,1}^{(bp)}(L_L)=\kappa_{x\,1}(L_L)\quad,\quad \left.\frac{d\kappa_{x\,1}^{(bp)}(x)}{dx}\right|_{x=L_L}=\left.\frac{d\kappa_{x\,1}(x)}{dx}\right|_{x=L_L} \tag{35c}$$

$$w_{0\,1}^{(bp)}(L_L)=w_{0\,1}(L_L)\quad,\quad \left.\frac{dw_{0\,1}^{(bp)}(x)}{dx}\right|_{x=L_L}=\left.\frac{dw_{0\,1}(x)}{dx}\right|_{x=L_L} \tag{35d}$$

(Application of continuity in axial displacement, curvature, and radial displacement, as well as their derivatives with respect to x, in the inner tube at x = L_L)

- At $x = L_L + L$;

$$N_{x\,1}(L_L+L)=0\quad,\quad M_{x\,1}(L_L+L)=0\quad,\quad Q_{x\,1}(L_L+L)=0 \tag{36a}$$

(Application of zero axial load/length, zero bending moment/length, and zero transverse shear load/length at the right face (free edge) of the inner tube, see Fig. 2)

$$u_{0\,2}(L_L+L)=u_{0\,2}^{(bp)}(L_L+L)\quad,\quad \left.\frac{du_{0\,2}(x)}{dx}\right|_{x=L_L+L}=\left.\frac{du_{0\,2}^{(bp)}(x)}{dx}\right|_{x=L_L+L} \tag{36b}$$

$$\kappa_{x\,2}(L_L+L)=\kappa_{x\,2}^{(bp)}(L+L)\quad,\quad \left.\frac{d\kappa_{x\,2}(x)}{dx}\right|_{x=L_L+L}=\left.\frac{d\kappa_{x\,2}^{(bp)}(x)}{dx}\right|_{x=L_L+L} \tag{36c}$$

$$w_{0\,2}(L_L+L)=w_{0\,2}^{(bp)}(L_L+L)\quad,\quad \left.\frac{dw_{0\,2}(x)}{dx}\right|_{x=L_L+L}=\left.\frac{dw_{0\,2}^{(bp)}(x)}{dx}\right|_{x=L_L+L} \tag{36d}$$

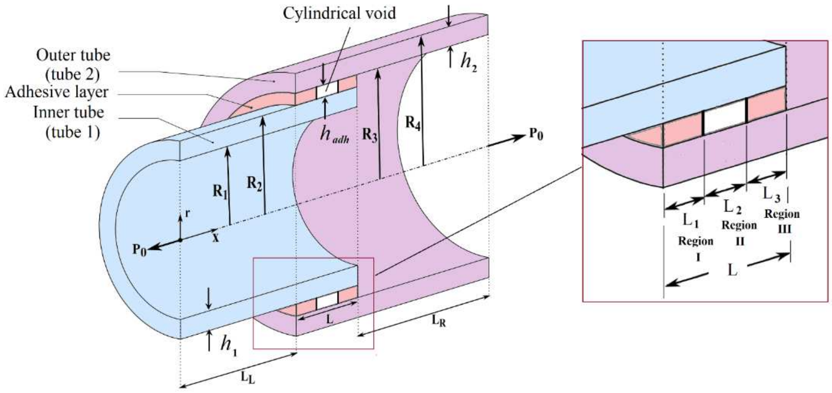

Fig. 5. The schematic diagram of a cylindrical tubular joint with a regional void.

(*Application of continuity in the axial displacement, curvature, and radial displacement of the outer tube, as well as their derivatives with respect to x, at* $x = L_L + L$, (*right end of the overlap region, see Fig.* 5)):

$$\sigma_{x,adh}(L_L + L) = 0 \tag{36e}$$

(*Application of zero normal stress at the right face (free edge) of the adhesive layer, see Fig.* 5)

- At $x = L_L + L + L_R$;

$$u_{0\,2}^{(bp)}(L_L + L + L_R) = 0 \ , \ \kappa_{x\,2}^{(bp)}(L_L + L + L_R) = 0 \ , \ w_{0\,2}^{(bp)}(L_L + L + L_R) = 0 \tag{37}$$

(*Application of end constraints at the right face of the outer tube*)

2.2. Governing differential equations for a defective tubular single lap joint hosting a cylindrical void

Figure 5 illustrates a tubular joint subjected to a tensile load with a cylindrical void. These defects often appear as cylindrical spaces, which can result from air bubbles trapped within the adhesive or from improper fabrication of the joint. The characteristics and behavior of these defects (void or debond) significantly differ from those of a crack. Therefore, the application of fracture mechanics in this context is not suitable. Instead, elasticity equations are used to derive the corresponding equations for stress distribution along the joint. In this context, linear elasticity can be employed for joint modeling (as in many other published investigations), provided that the peak stresses remain within their elastic limit. This method can effectively estimate the stress concentrations and stress distribution along the overlap of a joint, which in turn may be used in analyzing the joint failure if desired. Furthermore, in adhesives with viscoelastic properties, stresses are released over time. Thus, the peak stresses estimated by linear or nonlinear elasticity can facilitate a simpler determination of the adhesive's peak stresses (that occur at time zero) compared to employing a linear or nonlinear viscoelastic model for the adhesive layer.

On this basis, to derive the equilibrium equations, the bond length was divided into three regions with the lengths L_1, L_2, and L_3. Applying elasticity equations, equilibrium equations analogous to those for a defect-free joint (with length L) were derived for regions I and III of each tube (with the lengths L_1 and L_3 respectively). Although not shown, these equations were differentiated from those in the previous section using the superscripts (I) and (III). However, in region II, due to the lack of an adhesive (as a result of a void), the equilibrium equations were similar to those in Eqs. (6)-(8) except superscript (II) was used instead of "*bp*".

Applying the differential quadrature method in conjunction with the MATLAB software program, the solutions to these equations were determined according to the following fifty boundary and continuity conditions [32]. The distributions of shear and peel stresses at the adhesive-adherend interfaces were obtained accordingly [32].

- At $x = 0$:

$$N_{x\,1}^{(bp)}(0) = \frac{P_0}{2\pi\bar{R}_1},\ M_{x\,1}^{(bp)}(0) = 0,\ Q_{x\,1}^{(bp)}(0) = 0 \tag{38}$$

(*Application of axial load/length, zero bending moment/length, and zero transverse shear load/length at the left face of the inner tube, see Fig.* 5)

- At $x = L_L$:

$$N_{x\,2}^{(I)}(L_L) = 0,\ M_{x\,2}^{(I)}(L_L) = 0,\ Q_{x\,2}^{(I)}(L_L) = 0 \tag{39a}$$

(*Application of zero axial load/length, zero bending moment/length, and zero transverse shear load/length at the left face (free edge) of the outer tube* at the *beginning of the overlap region, see Fig.* 5)

$$\begin{gathered} u_{0\,1}^{(bp)}(L_L) = u_{0\,1}^{(I)}(L_L),\quad \kappa_{x\,1}^{(bp)}(L_L) = \kappa_{x\,1}^{(I)}(L_L)\ ,\quad w_{0\,1}^{(bp)}(L_L) = w_{0\,1}^{(I)}(L_L) \\ \left.\frac{du_{0\,1}^{(bp)}(x)}{dx}\right|_{x=L_L} = \left.\frac{du_{0\,1}^{(I)}(x)}{dx}\right|_{x=L_L},\ \left.\frac{d\kappa_{x\,1}^{(bp)}(x)}{dx}\right|_{x=L_L} = \left.\frac{d\kappa_{x\,1}^{(I)}(x)}{dx}\right|_{x=L_L}, \\ \left.\frac{dw_{0\,1}^{(bp)}(x)}{dx}\right|_{x=L_L} = \left.\frac{dw_{0\,1}^{(I)}(x)}{dx}\right|_{x=L_L} \end{gathered} \tag{39b}$$

(*Application of continuity in the axial displacement, curvature, and radial displacement of the inner tube, as well as their derivatives with respect to x, at the beginning of the overlap region* ($x = L_L$))

- At $x = L_L + L_1$:

$$u_{0\,1}^{(I)}(L_L + L_1) = u_{0\,1}^{(II)}(L_L + L_1) \tag{40a}$$

$$\kappa_{x\,1}^{(I)}(L_L + L_1) = \kappa_{x\,1}^{(II)}(L_L + L_1) \tag{40b}$$

$$w_{0\,1}^{(I)}(L_L + L_1) = w_{0\,1}^{(II)}(L_L + L_1) \tag{40c}$$

(*Application of continuity in the axial displacement, curvature, and radial displacement of the inner tube at the junction of regions I and II* ($x = L_L+L_1$))

$$\left.\frac{du_{0\,1}^{(I)}(x)}{dx}\right|_{x=L_L+L_1} = \left.\frac{du_{0\,1}^{(II)}(x)}{dx}\right|_{x=L_L+L_1} \tag{40d}$$

$$\left.\frac{d\kappa_{x\,1}^{(I)}(x)}{dx}\right|_{x=L_L+L_1} = \left.\frac{d\kappa_{x\,1}^{(II)}(x)}{dx}\right|_{x=L_L+L_1} \tag{40e}$$

$$\left.\frac{dw_{0\,1}^{(I)}(x)}{dx}\right|_{x=L_L+L_1} = \left.\frac{dw_{0\,1}^{(II)}(x)}{dx}\right|_{x=L_L+L_1} \tag{40f}$$

(*Application of continuity in derivatives of axial displacement, curvature, and radial displacement with respect to x of the inner tube at the junction of regions I and II* ($x = L_L+L_1$))

$$u_{0\,2}^{(I)}(L_L + L_1) = u_{0\,2}^{(II)}(L_L + L_1) \tag{40g}$$

$$\kappa_{x\,2}^{(I)}(L_L + L_1) = \kappa_{x\,2}^{(II)}(L_L + L_1) \tag{40h}$$

$$w_{0\,2}^{(I)}(L_L + L_1) = w_{0\,2}^{(II)}(L_L + L_1) \tag{40i}$$

(*Application of continuity in the axial displacement, curvature, and radial displacement of the outer tube at the junction of regions I and II (starting location of the void, see Fig.* 5))

$$\left.\frac{d\kappa_{x\,2}^{(I)}(x)}{dx}\right|_{x=L_L+L_1} = \left.\frac{d\kappa_{x\,2}^{(II)}(x)}{dx}\right|_{x=L_L+L_1} \tag{40j}$$

$$\left.\frac{du_{0\,2}^{(I)}(x)}{dx}\right|_{x=L_L+L_1} = \left.\frac{du_{0\,2}^{(II)}(x)}{dx}\right|_{x=L_L+L_1} \tag{40k}$$

$$\left.\frac{dw_{0\,2}^{(I)}(x)}{dx}\right|_{x=L_L+L_1} = \left.\frac{dw_{0\,2}^{(II)}(x)}{dx}\right|_{x=L_L+L_1} \tag{40l}$$

(*Application of continuity in derivatives of axial displacement, curvature, and radial displacement with respect to x of the outer tube at the junction of regions I and II (starting location of the void, see Fig.* 5))

$$\sigma_{x,adh}(L_L + L_1) = 0 \tag{40m}$$

(*Application of zero normal (axial) stress at the free surface of the adhesive layer due to the presence of a void*)

- At $x = L_L + L_1 + L_2$:

$$u_{0\,1}^{(I)}(L_L + L_1 + L_2) = u_{0\,1}^{(II)}(L_L + L_1 + L_2) \tag{41a}$$

$$\kappa_{x\,1}^{(I)}(L_L + L_1 + L_2) = \kappa_{x\,1}^{(II)}(L_L + L_1 + L_2) \tag{41b}$$

$$w_{0\,1}^{(I)}(L_L + L_1 + L_2) = w_{0\,1}^{(II)}(L_L + L_1 + L_2) \tag{41c}$$

(*Application of continuity in the axial displacement, curvature, and radial displacement of the inner tube at the junction of regions II and III (ending location of the void, see Fig.* 5))

$$\left.\frac{du_{0\,1}^{(I)}(x)}{dx}\right|_{x=L_L+L_1+L_2} = \left.\frac{du_{0\,1}^{(II)}(x)}{dx}\right|_{x=L_L+L_1+L_2} \tag{41d}$$

$$\left.\frac{d\kappa_{x\,1}^{(I)}(x)}{dx}\right|_{x=L_L+L_1+L_2}=\left.\frac{d\kappa_{x\,1}^{(II)}(x)}{dx}\right|_{x=L_L+L_1+L_2} \tag{41e}$$

$$\left.\frac{dw_{0\,1}^{(I)}(x)}{dx}\right|_{x=L_L+L_1+L_2}=\left.\frac{dw_{0\,1}^{(II)}(x)}{dx}\right|_{x=L_L+L_1+L_2} \tag{41f}$$

(Application of continuity in the derivatives of axial displacement, curvature, and radial displacement of the inner tube with respect to x at the junction of regions II and III (ending location of the void, see Fig. 5))

$$u_{0\,2}^{(I)}(L_L+L_1+L_2)=u_{0\,2}^{(II)}(L_L+L_1+L_2) \tag{41g}$$

$$\kappa_{x\,2}^{(I)}(L_L+L_1+L_2)=\kappa_{x\,2}^{(II)}(L_L+L_1+L_2) \tag{41h}$$

$$w_{0\,2}^{(I)}(L_L+L_1+L_2)=w_{0\,2}^{(II)}(L_L+L_1+L_2) \tag{41i}$$

(Application of continuity in the axial displacement, curvature, and radial displacement of the outer tube at the junction of regions II and III (ending location of the void, see Fig. 5))

$$\left.\frac{du_{0\,2}^{(I)}(x)}{dx}\right|_{x=L_L+L_1+L_2}=\left.\frac{du_{0\,2}^{(II)}(x)}{dx}\right|_{x=L_L+L_1+L_2} \tag{41j}$$

$$\left.\frac{d\kappa_{x\,2}^{(I)}(x)}{dx}\right|_{x=L_L+L_1+L_2}=\left.\frac{d\kappa_{x\,2}^{(II)}(x)}{dx}\right|_{x=L_L+L_1+L_2} \tag{41k}$$

$$\left.\frac{dw_{0\,2}^{(I)}(x)}{dx}\right|_{x=L_L+L_1+L_2}=\left.\frac{dw_{0\,2}^{(II)}(x)}{dx}\right|_{x=L_L+L_1+L_2} \tag{41l}$$

(Application of continuity in the derivatives of axial displacement, curvature, and radial displacement of the outer tube with respect to x, at the junction of regions II and III (ending location of the void, see Fig. 5))

- At $x=L_L+L_1+L_2+L_3$:

$$N_{x\,1}^{(III)}(L_L+L_1+L_2+L_3)=0 \tag{42a}$$

$$M_{x1}^{(III)}(L_L+L_1+L_2+L_{3L})=0 \tag{42b}$$

$$Q_{x1}^{(III)}(L_L+L_1+L_2+L_3)=0 \tag{42c}$$

(Application of zero axial load/length, zero bending moment/length, and zero transverse shear load/length at the right face (free face) of the inner tube, see Fig. 5)

$$u_{0\,2}^{(III)}(L_L+L_1+L_2+L_3)=u_{0\,2}^{(bp)}(L_L+L_1+L_2+L_3) \tag{42d}$$

$$\kappa_{x\,2}^{(III)}(L_L+L_1+L_2+L_3)=\kappa_{x\,2}^{(bp)}(L_L+L_1+L_2+L_3) \tag{42e}$$

$$w_{0\,2}^{(III)}(L_L+L_1+L_2+L_3)=w_{0\,2}^{(bp)}(L_L+L_1+L_2+L_3) \tag{42f}$$

(Application of continuity in the axial displacement, curvature, and radial displacement of the outer tube at the junction of region III with the remaining length of tube 2 characterized by L_R, see Fig. 5)

$$\left.\frac{du_{0\,2}^{(III)}(x)}{dx}\right|_{x=L_L+L_1+L_2+L_3}=\left.\frac{du_{0\,2}^{(bp)}(x)}{dx}\right|_{x=L_L+L_1+L_2+L_3} \tag{42g}$$

$$\left.\frac{d\kappa_{x\,2}^{(III)}(x)}{dx}\right|_{x=L_L+L_1+L_2+L_3}=\left.\frac{d\kappa_{x\,2}^{(bp)}(x)}{dx}\right|_{x=L_L+L_1+L_2+L_3} \tag{42h}$$

$$\left.\frac{dw_{0\,2}^{(III)}(x)}{dx}\right|_{x=L_L+L_1+L_2+L_3}=\left.\frac{dw_{0\,2}^{(bp)}(x)}{dx}\right|_{x=L_L+L_1+L_2+L_3} \tag{42i}$$

(Application of continuity in the derivative of axial displacement, curvature, and radial displacement with respect to x of the outer tube at the junction of region III with the remaining length of tube 2 characterized by L_R, see Fig. 5)

$$\sigma_{x,adh}(L_L+L_1+L_2+L_3)=0 \tag{42j}$$

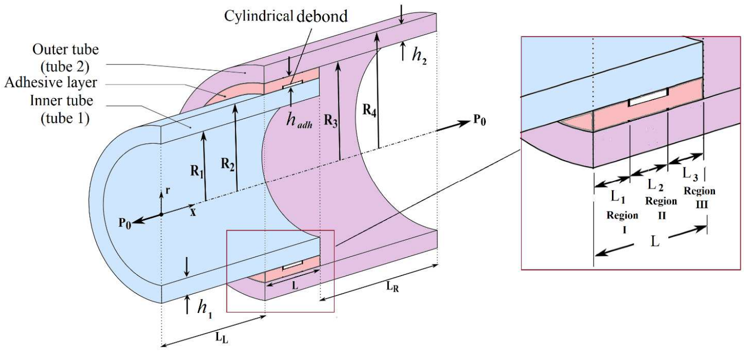

Fig. 6. The schematic diagram of a cylindrical tubular joint with a regional debond.

(*Application of zero normal stress at the right face (free edge) of the adhesive layer, see Fig. 5*)

- At $x = L_L + L_1 + L_2 + L_3 + L_R$:

$$u_{0\,2}^{(bp)}(L_L + L_1 + L_2 + L_3 + L_R) = 0 \tag{43a}$$

$$\kappa_{x\,2}^{(bp)}(L_L + L_1 + L_2 + L_3 + L_R) = 0 \tag{43b}$$

$$w_{0\,2}^{(bp)}(L_L + L_1 + L_2 + L_3 + L_R) = 0 \tag{43c}$$

(*Application of end constraints at the right face of the outer tube*)

2.3. Governing differential equations for a defective tubular single lap joint hosting a cylindrical debond

A tubular joint with a central partial debond between the adherend and inner tube is shown in Fig. 6. To derive the equilibrium equations, similar to a void defect, the bond length was divided into three regions I, II, and II, with the length L_1, L_2, and L_3, respectively. The equilibrium equations for regions I and III were similar to those extracted for a void defect except in region II, due to a partial debond between the adhesive and inner tube, the axial displacement function was selected according to Eq. (44) to allow for zero shear stress along the debond length:

$$u_{adh}^{(II)}(x,r) = \rho_0(r)u_0^{(II)}(x) + \rho_2(r)u_2^{(II)}(x) \tag{44}$$

Furthermore, in region II, $\tau_{rx,adh}^{(II)}(x,R_2) = 0.$ This condition can be written in terms of adhesive displacement components as:

$$G_{adh}\left(\frac{\partial u_{adh}^{(II)}(x,r)}{\partial r} + \frac{\partial w_{adh}^{(II)}(x,r)}{\partial x}\right)\Bigg|_{r=R_2} = 0 \tag{45}$$

Equating $w_{adh}^{(II)}(x, r = R_2)$ to zero, Eq. (45) is recast as:

$$\frac{\partial u_{adh}^{(II)}(x,r)}{\partial r}\Bigg|_{r=R_2} = 0 \tag{46}$$

Using Eq. (46) in combination with Eqs. (47a) and (47b), the two functions $\rho_0(r)$ and $\rho_2(r)$ are determined in terms of tube parameters, as shown in Eqs. (48a) and (48b):

$$u_{adh}^{(II)}(x,\bar{R}_{adh}) = u_0^{(II)}(x) \tag{47a}$$

$$u_{adh}^{(II)}(x,R_3) = u_2^{(II)}(x) \tag{47b}$$

$$\rho_0(r) = \frac{-r^2 - 2rR_2 + 2\bar{R}_aR_2 + \bar{R}_a^2}{(R_3 - \bar{R}_a)(\bar{R}_a + R_3 - 2R_2)} \tag{48a}$$

$$\rho_2(r) = \frac{r^2 - 2rR_2 + 2\bar{R}_aR_2 - \bar{R}_a^2}{(R_3 - \bar{R}_a)(\bar{R}_a + R_3 - 2R_2)} \tag{48b}$$

Using these relations, it can be shown that the expressions for the adhesive stresses in region II are [32]:

$$\sigma_{x,adh}^{(II)}(x,r) = E_{adh}\left(\rho_0(r)\frac{du_0^{(II)}(x)}{dx} + \rho_2(r)\frac{du_2^{(II)}(x)}{dx}\right) \tag{49a}$$

$$\sigma_{r,adh}^{(II)}(x,r) = 0 \tag{49b}$$

$$\tau_{rx,adh}^{(II)}(x,r)=G_{adh}\left(\frac{d\rho_0(r)}{dr}u_0^{(II)}(x)+\frac{d\rho_2(r)}{dr}u_2^{(II)}(x)+\frac{dw_{0\,2}^{(II)}(x)}{dx}\right) \tag{49c}$$

Moreover, by substituting Eq. (49a) into Eq. (28a) the axial load in the adhesive layer in region II is:

$$P_{x,adh}^{(II)}(x,r)=2\pi E_{adh}\int_{R_2}^{R_3}\left(\rho_0(r)\frac{du_0^{(II)}(x)}{dx}+\rho_2(r)\frac{du_2^{(II)}(x)}{dx}\right)rdr \tag{50}$$

This equation might be simplified as:

$$P_{x,adh}^{(II)}(x,r)=\xi_4\frac{du_0^{(II)}(x)}{dx}+\xi_5\frac{du_2^{(II)}(x)}{dx} \tag{51}$$

where,

$$\xi_4=2\pi E_{adh}\int_{R_2}^{R_3}\rho_0(r)\,rdr \tag{52a}$$

$$\xi_5=2\pi E_{adh}\int_{R_2}^{R_3}\rho_2(r)\,rdr \tag{52b}$$

The boundary and continuity conditions used to solve the resulting differential equations are similar to those introduced for the void model, except that Eq. (40m) is replaced with the following two conditions [25, 29]:

$$u_0^{(I)}(L_L+L_1)=u_0^{(II)}(L_L+L_1) \tag{53a}$$

(Satisfaction of continuity in adhesive displacement above the debond region at the junction of regions I and II)

$$u_0^{(II)}(L_L+L_1+L_2)=u_0^{(III)}(L_L+L_1+L_2) \tag{53b}$$

(Satisfaction of continuity in adhesive displacement above the debond region at the junction of regions II and III)

3. Finite Element Models of the Joint and Properties of the Selected Materials

To validate the results of semi-analytical solutions, a few models were prepared and solved using ABAQUS V2020 finite element engineering software. The models included three types of joints introduced before (namely, a perfect joint model, a defective joint with a void, and a joint hosting a debond). All models were exposed to an axial force that produced an axial stress of σ = 100 MPa in each tube outside the bond length, far enough from the overlap ends. To mesh the models, the 8-node C3D8R element with translational degrees of freedom at each node was selected for both the adhesive and adherends (see Figs. 7(a)-7(d)). To better estimate the stress concentrations at the zones with a high-stress gradient, the elements were reduced in size at locations near the overlap ends (for a defect-free joint) and at the free edges of the debond or the void (for a defective adhesive). To obtain accurate results, the reduced integral method was adopted to obtain the solutions.

To apply the axial load, a reference point was selected at the center of the cross-sectional area of the inner tube. Using the coupling constraint this point was integrated with the cross section to apply the load (on the left side) and boundary conditions on the right side of the model.

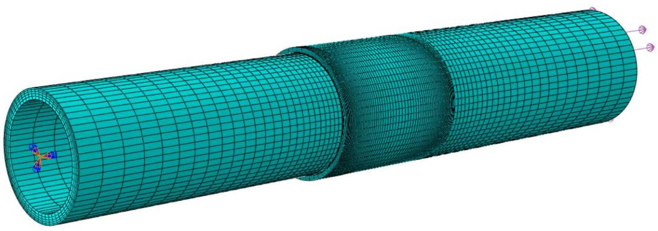

(a)

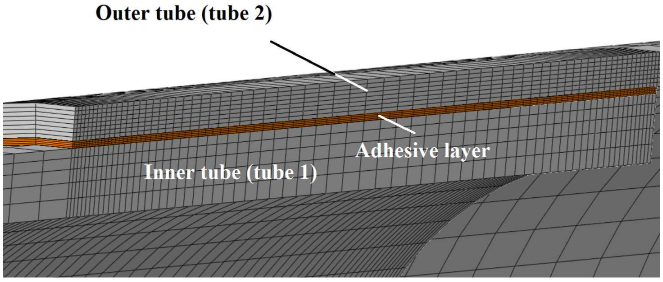

(b)

Fig. 7. Meshed models of the single lap joint and the convergence results used in the present analysis [32], (a) A meshed model of the tubular lap joint with the applied boundary conditions at the ends, (b) Meshed model of the bond length with no defect in the adhesive, (c) Meshed model of the bond length with a void in the adhesive, (d) Meshed model of the bond length with a debond in the adhesive, (e) Convergence test for the achievement of accurate results.

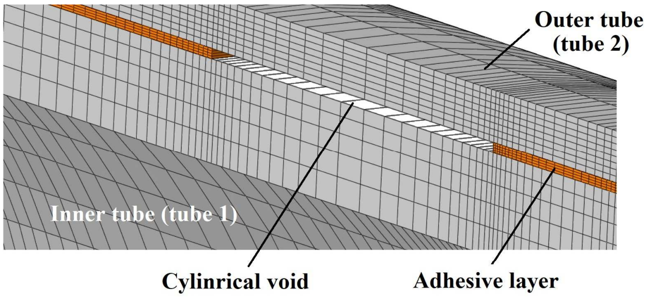

(c)

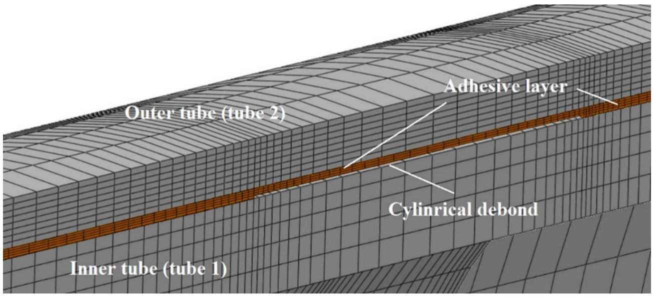

(d)

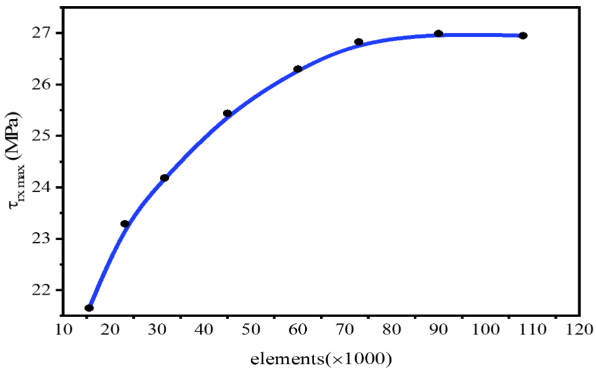

(e)

Fig. 7. Continued.

Table 1. Mechanical and geometric properties of the joint constituents (the inner tube and adhesive layer were assumed to be isotropic) [32].

Parameter	Outer tube (tube 2) (glass/epoxy)	Inner tube (tube 1) (Aluminum or steel)	Adhesive layer (IPCO 9923)
Inner radius (mm)	12.2	10.0	12.0
Outer radius (mm)	13.2	12.0	12.2
Total length (mm)	90.0 ($L+L_R$)	90.0 (L_L+L)	30.0 (L)
Elastic modulus E_1 (GPa)	26.2	75.0 (aluminum), 200 (steel)	2.5
Elastic modulus E_2 (GPa)	26.2	75.0 (aluminum), 200 (steel)	2.5
Elastic modulus E_3 (GPa)	11.6	75.0 (aluminum), 200 (steel)	2.5
Shear modulus G_{12} (GPa)	4.8	28.85 (aluminum), 80.6 (steel)	1.0
Shear modulus G_{13} (GPa)	2.6	28.85 (aluminum), 80.6 (steel)	1.0
Shear modulus G_{23} (GPa)	2.6	28.85 (aluminum), 80.6 (steel)	1.0
Poisson's ratio ν_{12}	0.1	0.3	0.35
Poisson's ratio ν_{13}	0.15	0.3	0.35
Poisson's ratio ν_{23}	0.2	0.3	0.35

4. Results and Discussions

4.1. Defect-free model

To verify the accuracy of formulations and the solution method adopted in this work, the results of the semi-analytical analysis for a defect-free *lap joint* were obtained and compared against the finite element results. The pertinent results were based on an axial force that produced a normal axial stress of σ = 100 MPa in each tube far enough from the bonded length.

As shown in Figs. 8(a) and 8(b), good agreements were obtained between the results of both methods for the interfacial shear stresses $\tau_{rx1} \equiv \tau_1$ and $\tau_{rx2} \equiv \tau_2$ (see Fig. 3). The end differences in the peak shear stress between the present semi-analytical results and those of finite element findings are due to singularity in the formulation of the problem that is based on the solid mechanics approach [26-27]. It is worth mentioning that the term "singularity" in joint analysis refers to the phenomenon where shear and peel stresses at the free adhesive ends (the overlap ends) exhibit a high-stress gradient over a short distance from the edges of the overlap region. Ideally, the free ends of the adhesive must experience zero shear and peel stress. However, in most joint analyses, applying the condition of zero shear and peel stress at these ends is challenging due to the complexity of the problem. This singularity arises from the structural mechanics (rather than continuum mechanics) approach typically adopted for problem formulation, which may be based on linear or nonlinear elasticity. Only a few studies have successfully implemented zero shear or peel stress as boundary conditions at the free ends of the adhesive layer (i.e., see Refs. [24, 28-30]). Since most solutions based on structural mechanics often fail to predict zero shear and peel stresses at the adhesive layer's free ends, alternative methods such as the finite element must be adopted to correct the stress values at these locations. However, despite the tendency of the solid *mechanics approach that uses elasticity equations to predict peel and shear stresses* along the bond length, application of this method usually leads to higher safety factors in joint analysis (due to higher shear and peel stresses), which may be desirable for a joint designer. Based on this argument, *numerous researchers have applied linear elasticity to obtain analytical or semi-analytical solutions* to present the distribution of stresses along the overlap length, while correcting the peak stresses (or stress concentrations) in the adhesive either by finite element analysis, analytical solutions, or an experimental work. Considering this argument, additional results on shear stress distribution in the adhesive layer of a *socket joint* under the *same axial load* were superimposed (from [24]) on the same graph to better differentiate between the shear stress distributions in a single lap joint and those of a *socket joint* (see Figs. 1(a) and 1(b)). In this comparison, the same physical and mechanical properties for the adherends and adhesive layers were used in both models. As observed, in the two types of joints, due to dissimilarities in the properties of the two tubes, the peak shear stresses at the adherend-adhesive interfaces occur at the right end of the joint. However, compared to the *single lap* joint, the *socket joint* in [24] experiences smaller values of peak shear stresses near the overlap right end due to its structural symmetry and loading about the y-z plane (see Fig. 1(b)). The reductions are about 25% for $\tau_{rx1} \equiv \tau_1$ and 35% for $\tau_{rx2} \equiv \tau_2$. Additionally, the peak values of shear stresses τ_1 and τ_2 that occur at the right end of the joint are the same in the *socket joint* model due to equality in tube diameters which is missing in a single-lap joint. As observed, for the *single lap* joint in the present work, due to the unequal diameters of the two tubes, $(\tau_{rx2})_{max} > (\tau_{rx1})_{max}$. As further investigations, the inner tube material was replaced with steel to explore the effect of any change in tube material on the adhesive shear and peel stress distributions. The pertinent results are superimposed on Figs. 8(a), and 8(b). As shown, replacing the inner aluminum tube with steel pipe slightly increases the peak shear stresses $(\tau_{rx1})_{max}$ and $(\tau_{rx2})_{max}$ that occur at the right end of the adhesive layer.

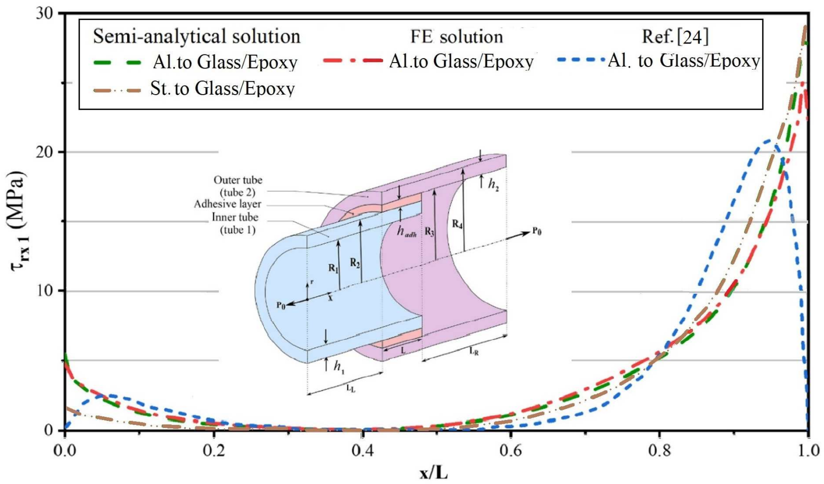

(a)

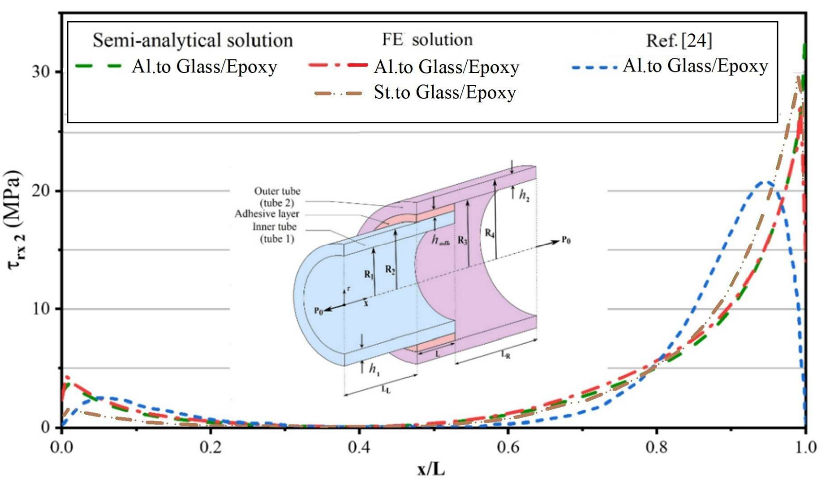

(b)

Fig. 8. Shear stress distributions at the adhesive-adherend interfaces in a defect-free tubular single lap joint under an axial tensile load ($[\pm 45_2]_S$ glass/epoxy outer tube) [32], (a) Distribution of shear stress at the lower adhesive-adherend interface, (b) Distribution of shear stress at the upper adhesive-adherend interface.

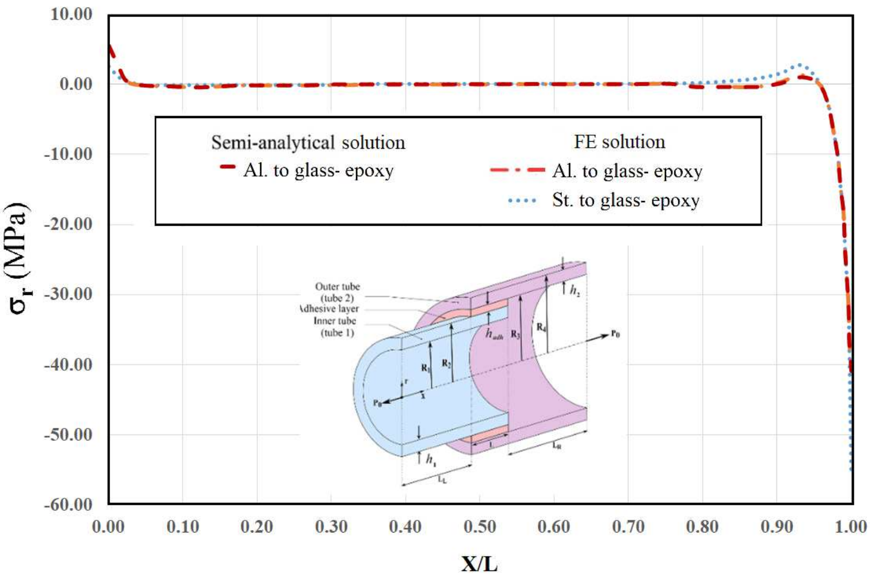

Fig. 9. Distribution of peel stress in the adhesive layer along the bond length ($[\pm 45_2]_S$ glass/epoxy outer tube).

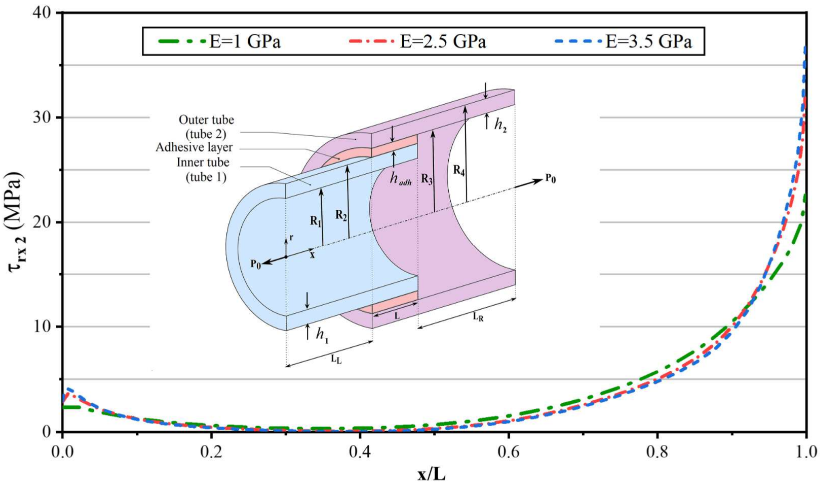

Fig. 10. Shear stress distribution at the adhesive–glass/epoxy ($[\pm 45_2]_S$) outer tube interface as a function of adhesive elastic modulus in a defect-free tubular single lap joint under axial tensile force [32].

Figure 9 presents the distribution of peel stress $\sigma \equiv \sigma_r$ in the adhesive layer along the bond length. As shown, there is a good agreement between the results of the finite element model and those of the semi-analytical solution. This validates the solution method and the assumptions made in formulating the problem. Based on the findings presented in this figure, it is observed that based on the geometric and mechanical properties selected for the joint, almost 80% of the bond length experiences zero peel stress, while this value is approximately 20% for the shear stresses at the adhesive-adherend interfaces. Furthermore, replacing the aluminum pipe with steel, reduced the tensile peel stress in the adhesive layer by 50%, due to the higher bending stiffness of the steel pipe.

Figure 10 shows the shear stress distribution at the adhesive-outer tube interface, as the elastic modulus of the adhesive layer increases from 1 GPa to 3.5 GPa. Similar behavior was observed for variation of $\tau_{rx1} \equiv \tau_1$ at the adhesive-inner tube interface, except that a smaller peak value of 32 MPa was observed at the right overlap end. According to these results, increasing the elastic modulus of the adhesive from 1 GPa to 3.5 GPa increases the adhesive peak shear stress by 54%. Although not shown, due to this increase in the elastic modulus, the tensile adhesive peel stress that occurred at the left end of the bond length, was increased from 3 MPa to 6.5 MPa, possessing a value of 5 MPa for E = 2.5 GPa.

Figures 11(a) and 11(b) show the distribution of shear and peel stresses along the bond length. According to the results in Fig. 11(a), there appears to be an optimum value of L for which the whole bond length remains active in bearing the shear load approaching zero at a location that is a function of geometric and mechanical properties of the joint's constituents. However, any changes in L appear to have a greater impact on the peak peel stress values $(\sigma_r)_{\max}$ in comparison with the peak shear stresses $(\tau_{rx1})_{\max}$ and $(\tau_{rx2})_{\max}$ (see Figs. 11(a) and 11(b)).

To explore the effect of lamination setup on the peel and shear stress distributions in the adhesive layer, in addition to the orthotropic lamination setups of $[+45_2/-45_2]_s$ and $[0_2/90_2]_S$, the quasi-isotropic arrangements of $[0/90/-45/45]_S$, and the transversely isotropic arrangement of $[0_8]$ were selected for the outer tube (see Figs. 12(a), 12(b), and 12(c)). However, to generate more meaningful differences in results due to a change in material properties and lamination setup, the inner tube was considered aluminum with carbon–epoxy composite as the outer tube. The corresponding mechanical properties of the outer tube are given in Table 2. In *all cases*, the total thickness of the carbon/epoxy composite pipe was assumed *to be constant* and equal to 1 mm. Using this value, each layer possessed a thickness of 0.125 mm. Other properties of the inner tube and the adhesive layer were selected according to Table 1.

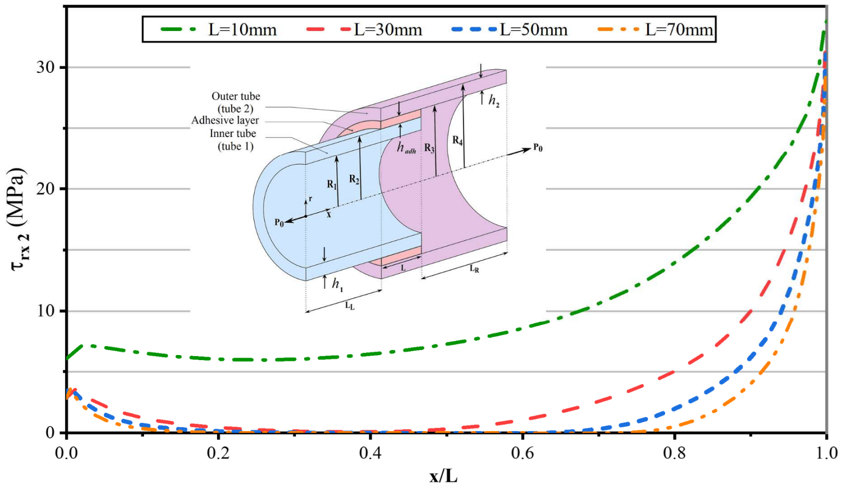

(a)

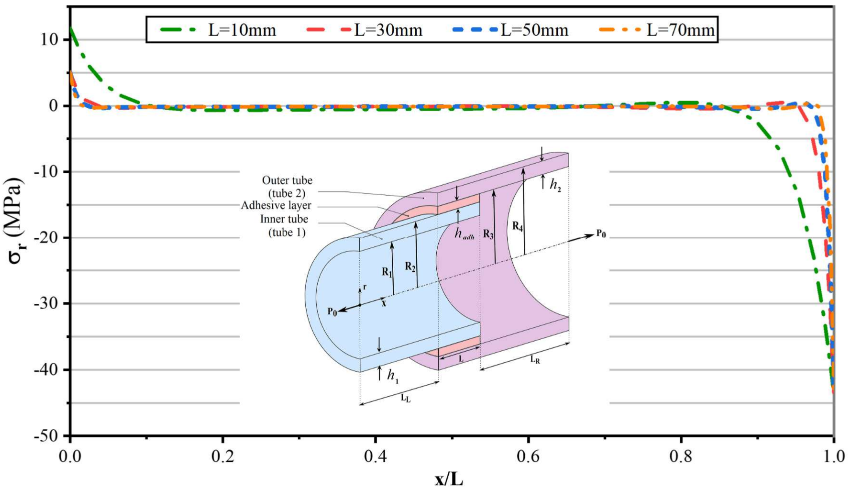

(b)

Fig. 11. Shear and peel stress distributions in the adhesive layer as a function of bond length in a defect-free tubular single-lap joint under an axial tensile load ($[\pm45_2]_S$ glass/epoxy outer tube) [32], (a) Distribution of shear stress at the adhesive-adherend interface, (b) Distribution of peel stress.

As shown in Fig. 12(a), the highest adhesive peak shear stress has occurred for the quasi-isotropic lamination setups of $[0/90/-45/45]_S$. However, in comparison with the orthotropic layer arrangements of $[0_2/90_2]_S$, the $[+45_2/-45_2]_s$ lamination sequence experienced smaller peak shear stresses at the two ends of the overlap region. According to Fig. 12(b), a similar behavior was observed for $(\tau_{rx2})_{max}$ with almost the same peak values as $(\tau_{rx1})_{max}$ near the overlap ends. Examination of the results in Fig. 12(c) indicates that although the quasi-isotropic arrangement of $[0/90/-45/45]_S$ created the highest interfacial peak stress in the adhesive layer, yet the highest positive peel stress experienced by this setup was very close to those of other layer sequences. Furthermore, as expected, the transversely isotropic lamination set of $[0_8]$ produces the best distribution for the peel stress, due to an applied tensile load. Nonetheless, considering the results in Figs. 12(a), 12(b), and 12(c), it is obvious that the $[0_8]$ arrangement seems to be the best choice for the arrangement of the layers in the composite pipe.

4.2. Defective adhesive hosting a cylindrical void

Figures 13(a) and 13(b) show the distribution of shear stresses τ_1 and τ_2 at the adhesive-adherend interfaces, in a defective joint hosting a void. To obtain these results, the void was assumed to have a length of L_2 = 8 mm at a location with L_1 = 18 mm, and L_3 = 4 mm. Furthermore, the properties of both tubes and the adhesive layer (in both sections 4.2 and 4.3) were selected from Table 1. Comparison of the results in Figs. 13(a) and 13(b) show similar distributions for τ_1 and τ_2 along the bond length except that $(\tau_{rx2})_{max} > (\tau_{rx1})_{max}$ at both ends of the overlap region. Furthermore, a comparison of the results in Figs. 13(b) and those in Fig. 8(b) indicate that the presence of the previously described void which is 26.6% of the total bond length, causes a 6.0 % increase in the maximum $(\tau_{rx2})_{max}$ that occurs at the right end of the bond length. However, although not shown, further investigation in results revealed that the impact of *central voids* (voids being centrally located along the bond length) on the peak shear stresses is only significant for void lengths exceeding 75% of the total bond length [32].

Table 2. Properties of the carbon/epoxy composite tube (total bond length = 60.0 mm).

Elastic modulus (GPa)			Shear modulus (GPa)			Poisson's ratio		
E_1	E_2	E_3	G_{12}	G_{13}	G_{23}	ν_{12}	ν_{13}	ν_{23}
128.0	10.0	10.0	4.49	4.49	3.58	0.28	0.28	0.47

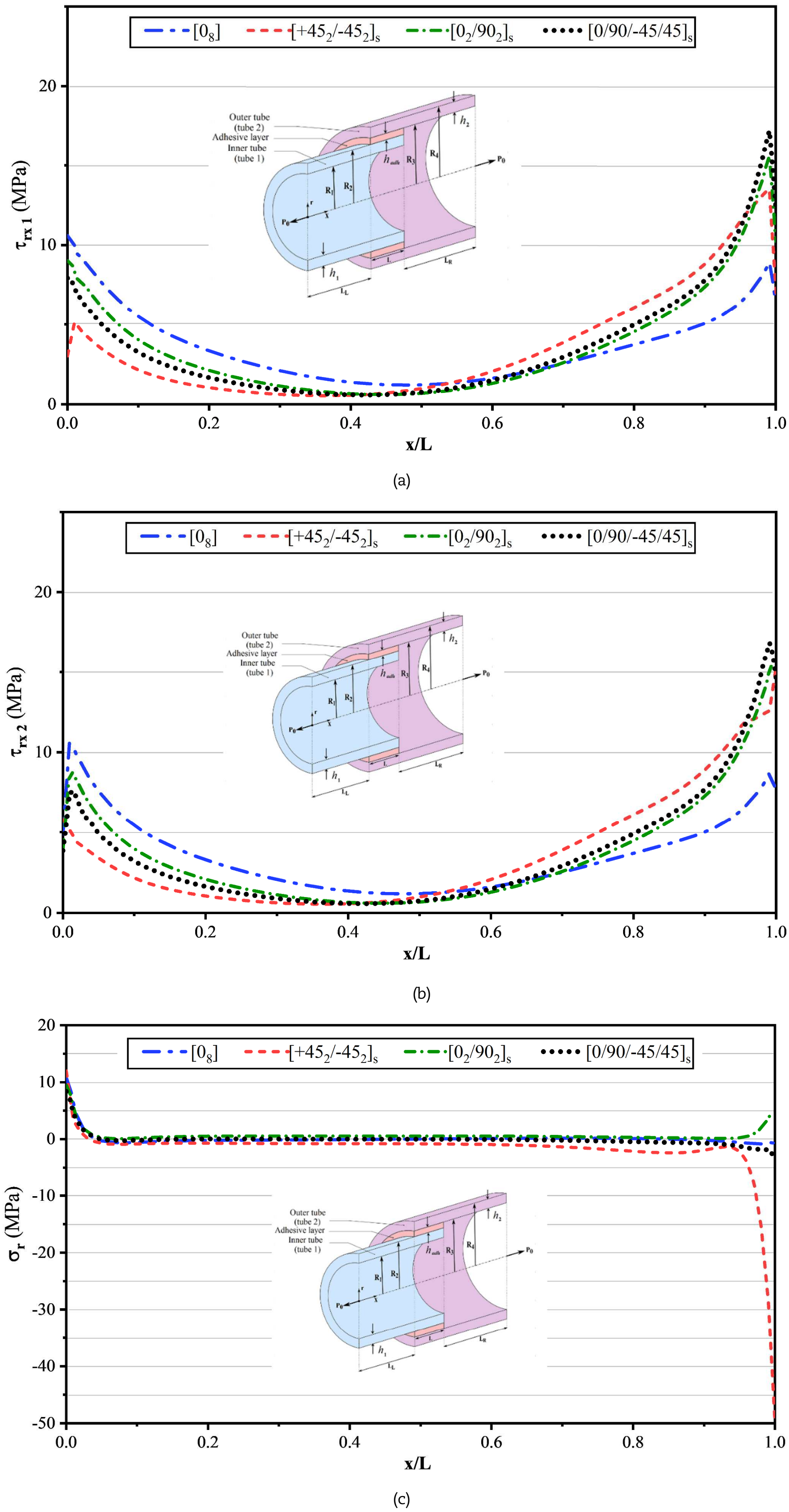

Fig. 12. Shear and peel stress Distributions as a function of lamination sequence (carbon/epoxy outer tube) along the bond length of a defect-free tubular single lap joint [32], (a) Shear stress distribution on the upper surface of the adhesive layer, (b) Shear stress distribution on the lower surface of the adhesive layer, (c) Peel stress distribution in the adhesive layer.

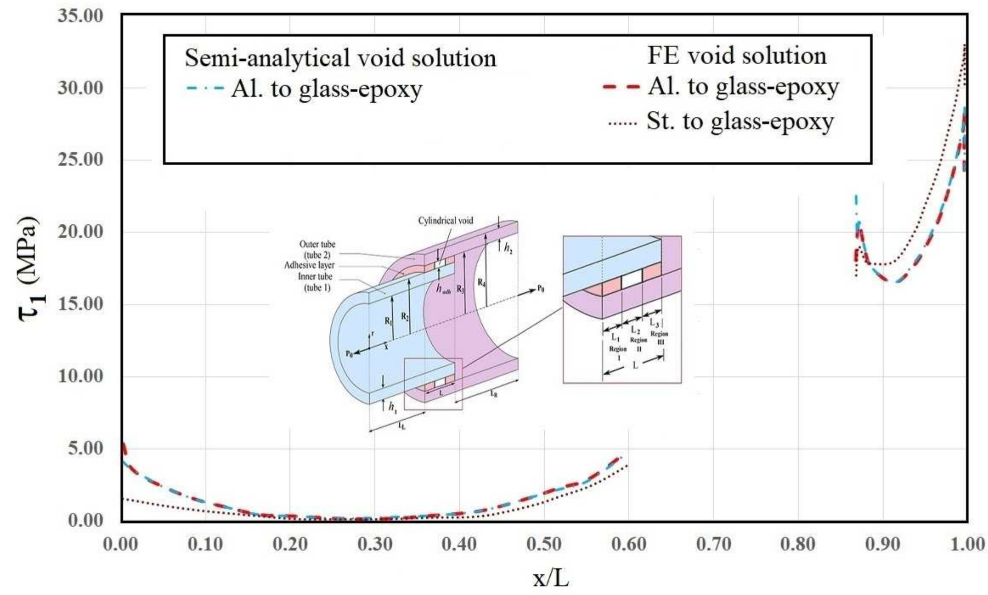

(a)

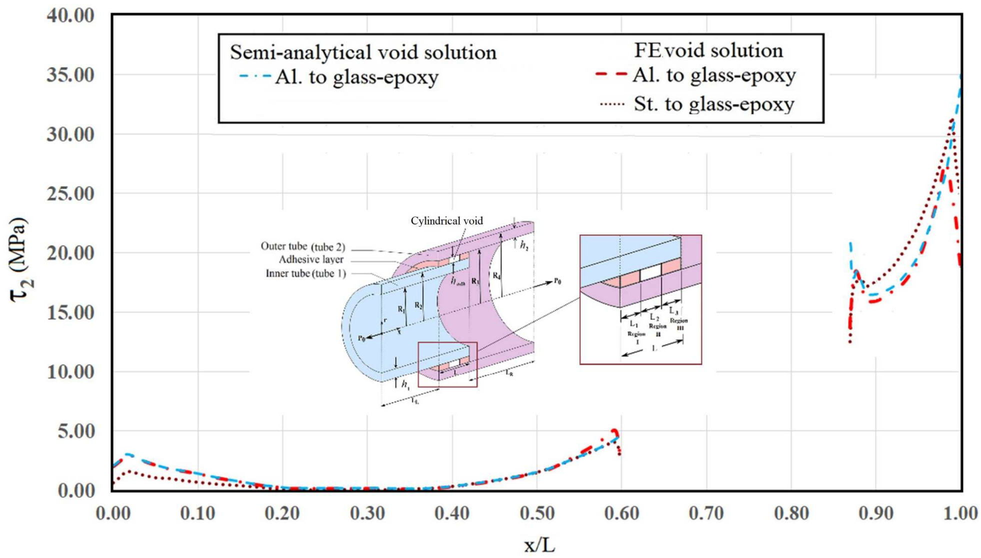

(b)

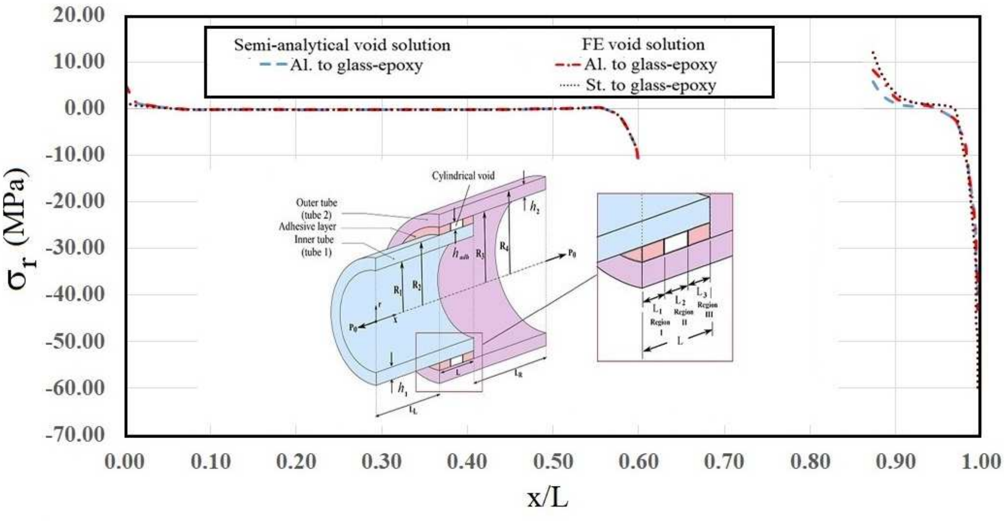

(c)

Fig. 13. Shear and peel stress distribution along the bond length (L=30 mm) in a tubular joint hosting a void and sustaining an axial tensile force ($[\pm45_2]_S$ glass/epoxy outer tube) [32], (a) Shear stress distribution on the lower surface of the adhesive layer, (b) Shear stress distribution on the upper surface of the adhesive layer, (c) Peel stress distribution along the bond length.

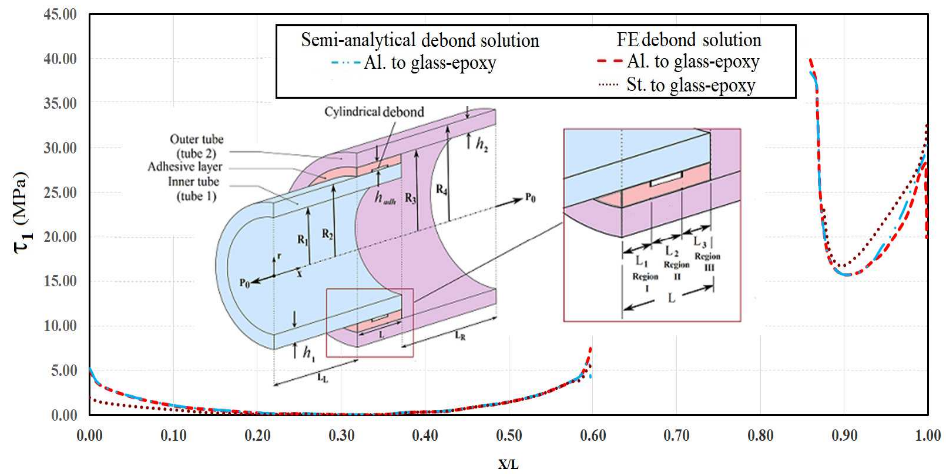

(a)

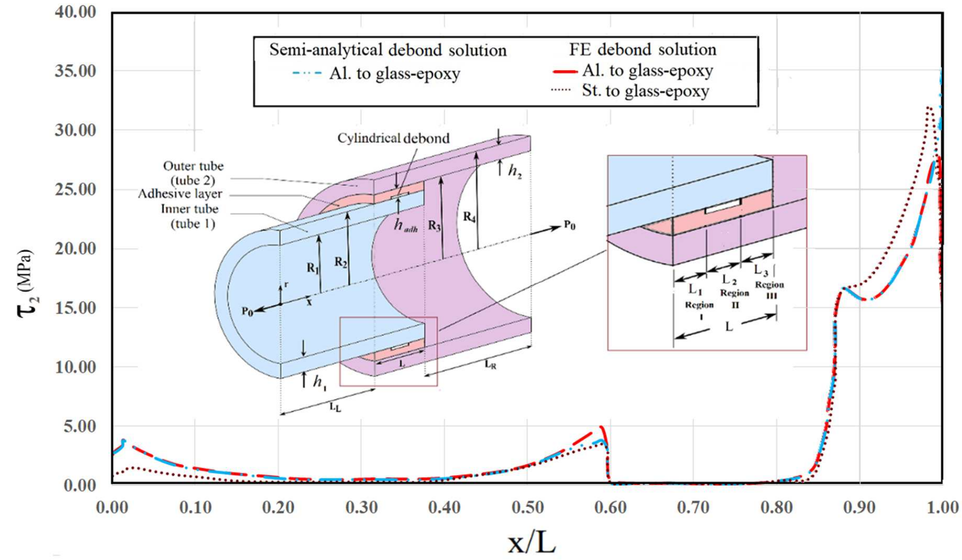

(b)

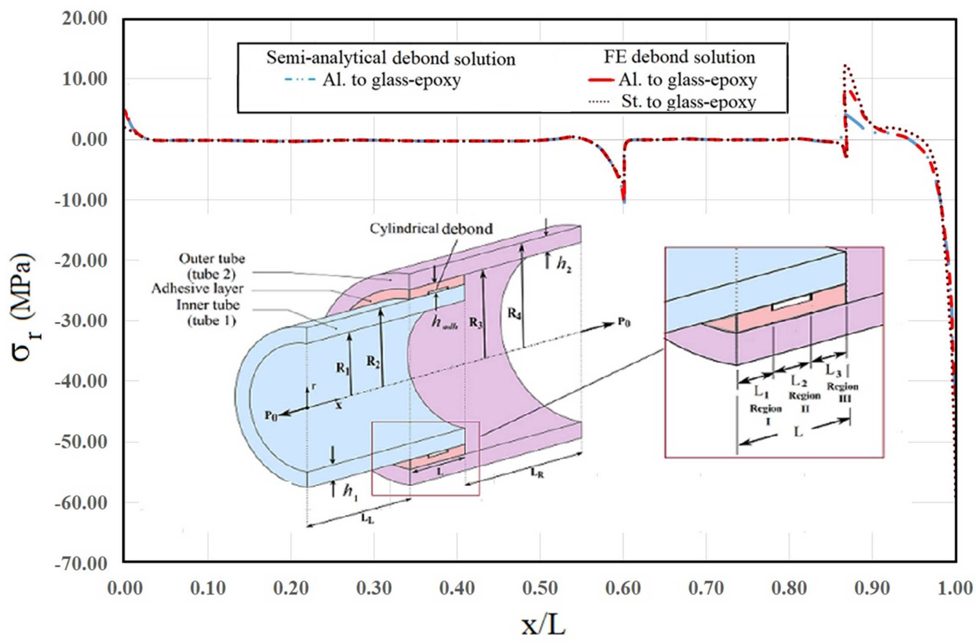

(c)

Fig. 14. Shear and peel stress distributions in a defective adhesive hosting a regional debond and sustaining an axial tensile force ($[\pm 45_2]_S$ glass/epoxy outer tube) [32], (a) Shear stress distribution on the adhesive layer's lower surface, (b) Shear stress distribution on the adhesive layer's upper surface, (c) Peel stress distributions in the adhesive layer along the bond length.

Analyzing the results in Fig. 13(c), it is evident that for the selected void dimension and location, *the highest positive peel stress occurs at the right edge of the void*, instead of *the left end of the bond length,* as is the case for a defect-free adhesive layer (see Fig. 9). Additionally, based on an elastic modulus of 2.5 MPa for the adhesive layer, this indicates a 60% increase in the peel stress in comparison with a defect-free joint under similar loading condition.

To further investigate the effects of any change in tube material on stress distribution in a defective adhesive joint hosting a regional void, the aluminum inner tube was replaced with a steel pipe of the same size. The pertinent results were superimposed on Figs. 13(a), 13(b), and 13(c). As shown in Figs. 13(a) and 13(b), replacing the inner aluminum pipe with a steel tube, increases the peak shear stress $(\tau_{rx1})_{\max}$ by 18% and $(\tau_{rx2})_{\max}$ by 18.9% without affecting their locations. However, the tensile peel stress at the same location was increased by 44%.

4.3. Defective adhesive hosting a debond

Figures 14(a), 14(b), and 14(c) show similar distributions for the shear and peel stress components in the adhesive layer due to the presence of a debond with L_2 = 8 mm (L_1 = 18 mm, and L_3 = 4 mm). The finite element results were superimposed to verify the semi-analytical solution. According to Fig. 14(a), for the selected debond length and position, the peak shear stress $(\tau_{rx1})_{\max}$ occurs at *the right end of the debond surface* at its *lower interface*. This result is in contrast to the results of a defect-free (see Fig. 8(a)) and a defective joint hosting a void (see Fig. 13(a)), where the peak shear stress occurred at the right end of the overlap region. This indicates a 38% increase in $(\tau_{rx1})_{\max}$ compared to a defect-free joint. However, in comparison to a void, the presence of a debond in the adhesive layer bonded to an aluminum inner tube shifts the location and magnitude of $(\tau_{rx1})_{\max}$ from 28 MPa at the right end of the overlap region (see Fig. 13(a)) to a value of 38.5 MPa at the right end of the debond surface (see Fig. 14(a)). This corresponds to a 39% rise in $(\tau_{rx1})_{\max}$. Moreover, a comparison of the results in Figs. 8(b), 13(b), and 14(b) indicate that the presence of previously described local defects (a void or a debond) in the adhesive layer, slightly increases $(\tau_{rx2})_{\max}$ without changing its location. According to the findings in reference [32], defects located near the right end of the overlap region had a more significant impact on the peak shear stresses. Additionally, a comparison of the results in Figs. 13(c) and 14(c) show that the peak positive peel stress developed in the adhesive layer due to a void is similar to that resulting from a debond.

To investigate the impact of material change on stress distribution in the adhesive layer, additional plots were overlaid on Figs. 14(a), (b), and (c), showing the effect of a steel pipe on stress shear and peel stress components. According to the finite element results, the use of a steel pipe had a dual impact on τ_1. Firstly, it increased the peak value of this stress from a value of 28 MPa to a value of 33 MPa at the right end of the overlap region; and secondly, it considerably reduced the peak value of $(\tau_{rx1})_{\max}$ from 39.5 MPa (based on the aluminum inner tube) to 23.5 MPa. This indicates a 40% reduction in the original $(\tau_{rx1})_{\max}$ based on the application of steel pipe. These results indicate this substitution in material can shift the magnitude and location of $(\tau_{rx1})_{\max}$ from the right end of the local debond to a location near the right end of the overlap region. However, an examination of Fig. 14(c) indicates that the tensile peak peel stress is increased by 44%, without any change in its location.

4.4. The effect of the outer tube's lamination sequence on the shear and peel stress distributions in a defective adhesive layer

4.4.1. *Defect as a void*

To explore the effect of lamination setup on the shear and peel stress distributions in a defective adhesive layer, three types of lamination setups, namely transversely isotropic, orthotropic, and quasi-isotropic arrangements were selected for the outer tube with carbon/epoxy as the pipe material. These setups were the same as those adopted in Fig. 12 for a defect-free joint. Figures 15(a), 15(b), and 15(c) show the corresponding distributions for τ_1, τ_2, and σ_r. As shown earlier in Figs. 13(a), (b), and (c), for a defective adhesive hosting a void, the application of $[\pm 45_2]_s$ layer arrangement for the outer glass/epoxy tube resulted in the peak shear stresses of $(\tau_{rx1})_{\max}$ and $(\tau_{rx2})_{\max}$ with the magnitudes of 31 MPa and 35 MPa, respectively, and a peak tensile peel stress of 8 MPa. However, if carbon/epoxy is used instead of glass/epoxy, according to Figs. 15(a), (b), and (c), for the same void size and location, values of 24 MPa, 23 MPa, and –3 MPa (negative peel stress) were obtained for the preceding stress values, respectively. These values show the positive effect of carbon/epoxy material over the glass/epoxy on improving both stress components in the adhesive layer. Furthermore, comparing the results in Fig. 15, it is evident that the $[0_8]$ transversely isotropic carbon/epoxy outer tube reduces the peak shear stresses $(\tau_{rx1})_{\max}$ and $(\tau_{rx2})_{\max}$ from 24 and 23 MPa to 8 MPa, marking a 200% reduction. This arrangement also contributes to a more uniform distribution of shear stresses, evening out the differences in shear stress values at the right ends of the overlap region and the debond. This ultimately results in a safer structure.

Additional comparison of the results in Figs. 13(c) and 15(c) shows that compared to the $[\pm 45_2]_s$ arrangement for the glass/epoxy, the application of carbon/epoxy for the outer tube shifts the peak value of tensile peel stress from *the void's right end* to the *left end of the overlap region*. Additionally, among the four different lamination setups of $[+45_2/-45_2]_s$, $[0_8]$, $[0/90/-45/45]_s$, and $[0_2/90_2]_s$ for the carbon/epoxy outer tube, the highest reduction in the peak adhesive tensile peel stress is achieved for the orthotropic arrangement of $[+45_2/-45_2]_s$, as it lowers the tensile $(\sigma_r)_{\max}$ by 41% (see Fig. 15(c)).

4.4.2. *Defect as a debond*

The effects of carbon/epoxy lamination setup on the shear and peel stress distributions in the adhesive layer hosting a regional debond are shown in Figs. 16(a), (b), and (c). The debond size, location, and layer sequences were the same as those selected for a void. Comparison of the results in Figs. 14(a), 14(b), and 14(c), and those in Figs. 16(a), 16(b), and 16(c), for the layer arrangement of $[\pm 45_2]_s$ shows that compared to glass epoxy, the application of carbon epoxy lowers the peak shear stresses $(\tau_{rx1})_{\max}$ and $(\tau_{rx2})_{\max}$ by 32%, 36%. Meanwhile, the peak tensile peel stress $(\sigma_r)_{\max}$ is reduced by 25%. Moreover, a comparison in results for different layer arrangements indicates that the use of transversely isotropic layer arrangement of $[0_8]$ is the best choice for the reduction of peak shear stresses as it lowers $(\tau_{rx1})_{\max}$ and $(\tau_{rx2})_{\max}$ by 57% and 56%, respectively, compared to $[+45_2/-45_2]_s$ setup. However, for the peak tensile peel stress, the application of $[+45_2/-45_2]_s$ arrangement seems to be a better choice for the outer tube since it mostly reduces the peak tensile peel stress compared to the other setups.

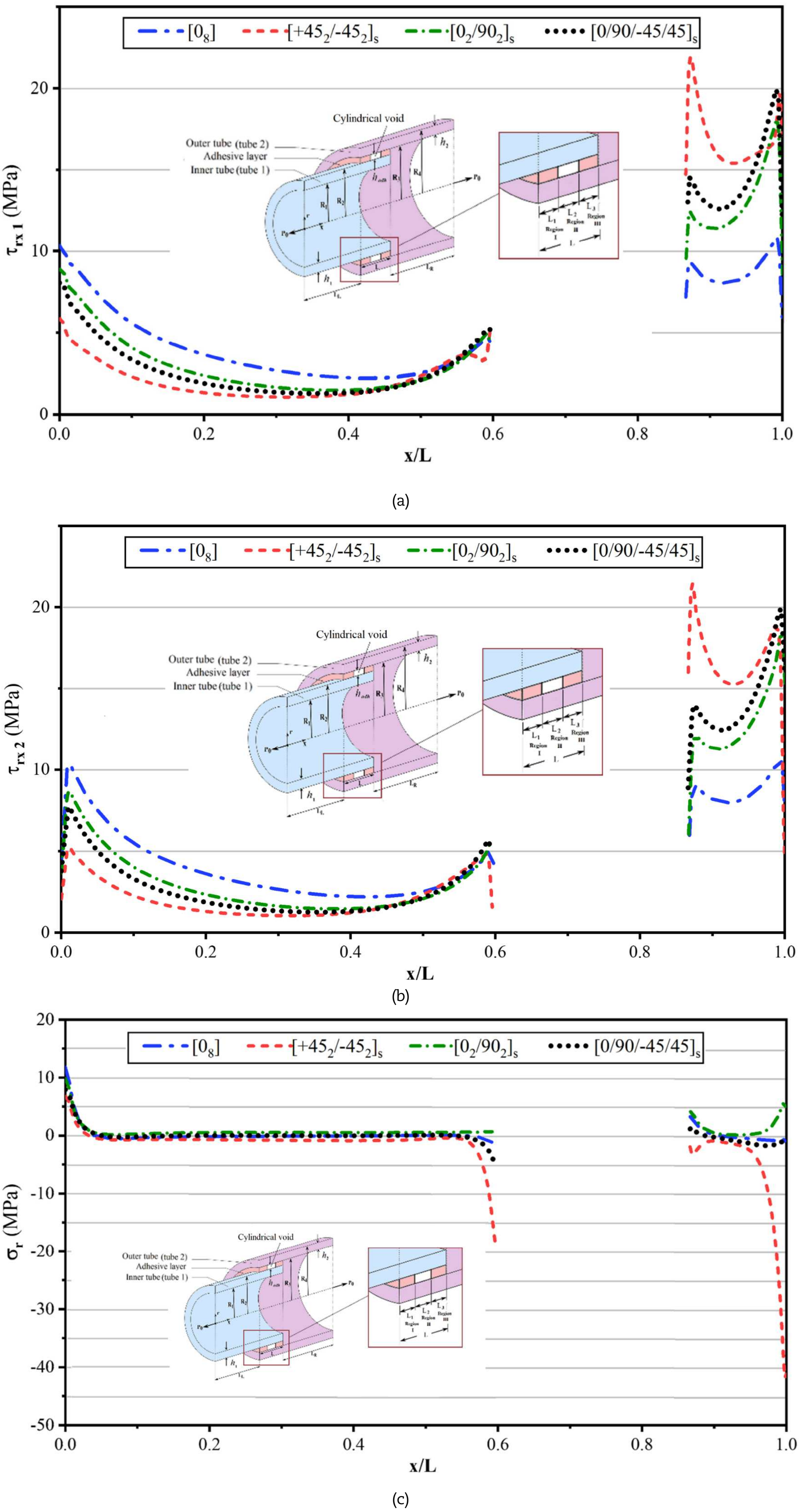

Fig. 15. The effect of lamination setup on the shear and peel stress distributions along the bond length in the adhesive layer of a tubular joint hosting a void and sustaining an axial tensile force (carbon/epoxy outer tube) [32], (a) Shear stress distribution on the lower surface of the adhesive layer, (b) Shear stress distribution on the upper surface of the adhesive layer, (c) Peel stress distribution in the adhesive layer.

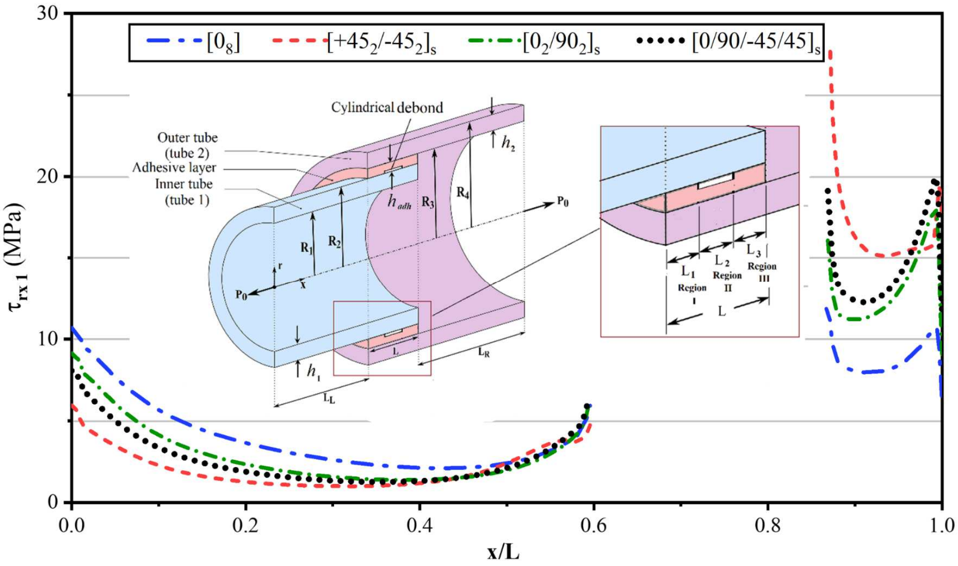

(a)

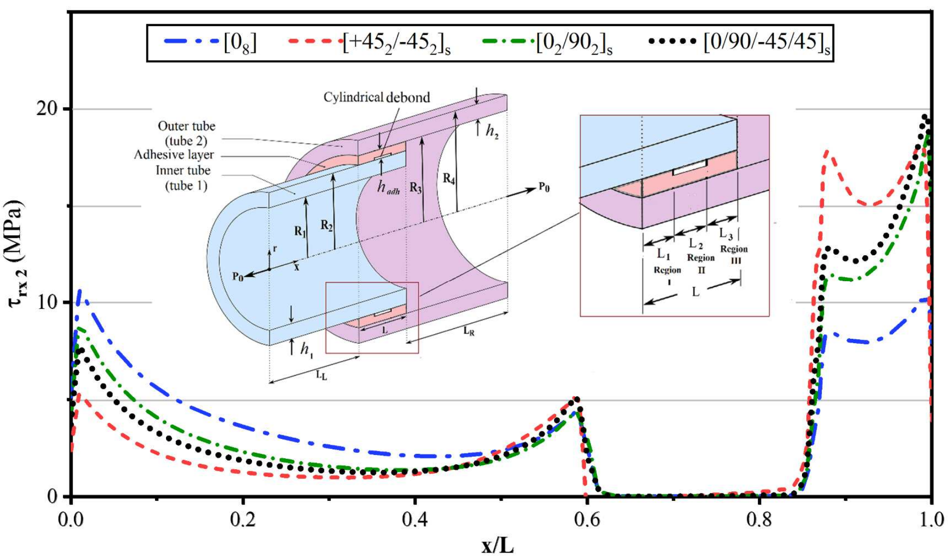

(b)

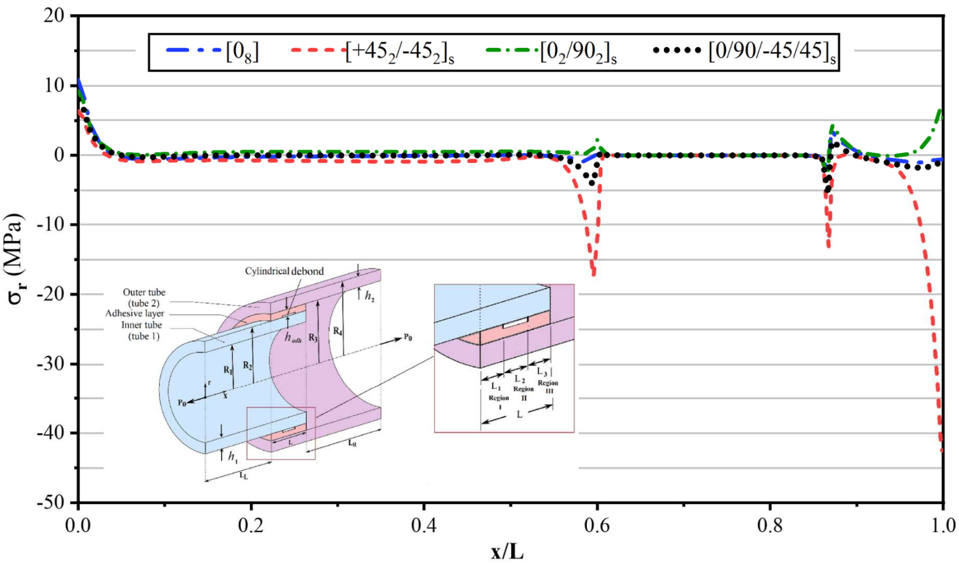

(c)

Fig. 16. The effect of lamination setup on the shear and peel stress distributions along the adhesive bond length of a tubular joint hosting a debond and sustaining an axial tensile force (carbon/epoxy outer tube) [32], (a) Shear stress distribution at the lower surface of the adhesive layer, (b) Shear stress distribution at the upper surface of the adhesive layer, (c) Peel stress distribution in the adhesive layer.

5. Conclusions

The present study examined how an adhesive defect and the adherend material can affect stress distribution in laminated composite tubular joints with axial tensile load. The tubular joint in question comprised two hollow tubes joined by a layer of adhesive to create a simple lap joint, bearing a local cylindrical defect as void or debond. The adherends were assumed to be either isotropic, quasi-isotropic, orthotropic, or transversely isotropic. Applying linear elasticity, the equilibrium equations were derived and solved using the differential quadrature method and MATLAB engineering software. Additionally, several finite element models of the joint were prepared and solved to validate the semi-analytical solutions. The results from both methods showed good agreement. Furthermore, the results on a defect-free single lap joint showed that compared to a socket joint in tension, the single lap joint experiences higher peak shear stresses near the overlap ends. Moreover, replacing the inner aluminum tube with a steel pipe slightly increases the peak shear stresses $(\tau_{rx1})_{\max}$ and $(\tau_{rx2})_{\max}$; although for this change in material and the selected joint geometry, the tensile peel stress in the adhesive layer was reduced by 50%, due to the higher bending stiffness of the steel pipe. According to the results, for a defect-free joint, among the orthotropic lamination setups of $[+45_2/-45_2]_S$ and $[0_2/90_2]_S$, the quasi-isotropic arrangements of $[0/90/-45/45]_S$, and the transversely isotropic arrangement of $[0_8]$, the lamination setup of $[0_8]$ for the carbon/epoxy outer tube produced the best distribution of peel stress with the least peak shear stresses compared to the other layer arrangements. Further results on a defective joint indicated that the existence of a void amplifies the maximum shear stress within the adhesive layer, along with a notable rise in the intensity of the peel stress, in addition to a shift in its location. The increase in $(\sigma_r)_{\max,\, tensile}$ was 60% for the void size at a location under consideration. Moreover, a local debond shifted the location of $(\tau_{rx1})_{\max}$ from the right end of the overlap region to the right end of the debond with a 39% increase in magnitude. Additional results indicate that in tubular joints with defects, the magnitudes and locations of the peak shear stresses $(\tau_{rx1})_{\max}$ and $(\tau_{rx2})_{\max}$, as well as peak tensile stress considerably depend on the material and/or lamination setup of the tubes. These results can serve as important guidelines in failure analysis of adhesively bonded tubular joints as they provide valuable insights into the root causes of joint failures and potential solutions for prevention.

Author Contributions

M. Shishesaz planned the scheme, initiated the project, and suggested the theoretical scheme; A.H. Ghamarian conducted the theoretical work and analyzed the empirical results under M. Shishesaz supervision; R. Mosalmani examined the theory validation and proposed necessary recommendation. The manuscript was written through the contribution of all authors. All authors discussed the results, reviewed, and approved the final version of the manuscript.

Acknowledgments

Not applicable.

Conflict of Interest

The authors declared no potential conflicts of interest concerning the research, authorship, and publication of this article.

Funding

Shahid Chamran University of Ahvaz supported this work under grant No. SCU.EM1400.561.

Data Availability Statements

The datasets generated and/or analyzed during the current study are available from the corresponding author on reasonable request.

Appendix A

Constant coefficients used in Eqs. (33a)-(33L) are:

$$J_1 = A_{11}^{(1)} + \frac{1}{\bar{R}_1}B_{11}^{(1)},\quad J_2 = B_{11}^{(1)} + \frac{1}{\bar{R}_1}D_{11}^{(1)},\quad J_3 = \frac{A_{12}^{(1)}}{\bar{R}_1} + \frac{R_2G_{adh}}{\bar{R}_1},\quad J_4 = \frac{R_2G_{adh}}{\bar{R}_1}\left(\frac{d\eta_1(r)}{dr} - \frac{\eta_1(r)}{r}\right)_{r=R_2},\quad J_5 = \frac{R_2G_{adh}h_1}{2\bar{R}_1}\left(\frac{d\eta_1(r)}{dr} - \frac{\eta_1(r)}{r}\right)_{r=R_2}, \tag{A.1}$$

$$J_6 = \frac{R_2G_{adh}}{\bar{R}_1}\left(\frac{d\eta_2(r)}{dr} - \frac{\eta_2(r)}{r}\right)_{r=R_2},\quad J_7 = -\frac{R_2G_{adh}h_2}{2\bar{R}_1}\left(\frac{d\eta_2(r)}{dr} - \frac{\eta_2(r)}{r}\right)_{r=R_2},\quad J_8 = \frac{R_2G_{adh}}{\bar{R}_1}\left(\frac{d\eta_0(r)}{dr} - \frac{\eta_0(r)}{r}\right)_{r=R_2},\quad J_9 = A_{11}^{(2)} + \frac{1}{\bar{R}_2}B_{11}^{(2)},\quad J_{10} = B_{11}^{(2)} + \frac{1}{\bar{R}_2}D_{11}^{(2)}, \tag{A.2}$$

$$J_{11} = \frac{A_{12}^{(2)}}{\bar{R}_2} - \frac{R_3G_{adh}}{\bar{R}_2},\quad J_{12} = -\frac{R_3G_{adh}}{\bar{R}_2}\left(\frac{d\eta_1(r)}{dr} - \frac{\eta_1(r)}{r}\right)_{r=R_3},\quad J_{13} = -\frac{R_3G_{adh}h_2}{2\bar{R}_2}\left(\frac{d\eta_1(r)}{dr} - \frac{\eta_1(r)}{r}\right)_{r=R_3},\quad J_{14} = -\frac{R_3G_{adh}}{\bar{R}_2}\left(\frac{d\eta_2(r)}{dr} - \frac{\eta_2(r)}{r}\right)_{r=R_3}, \tag{A.3}$$

$$J_{15} = \frac{R_2G_{adh}h_2}{2\bar{R}_1}\left(\frac{d\eta_2(r)}{dr} - \frac{\eta_2(r)}{r}\right)_{r=R_3},\quad J_{16} = -\frac{R_3G_{adh}}{\bar{R}_2}\left(\frac{d\eta_0(r)}{dr} - \frac{\eta_0(r)}{r}\right)_{r=R_3},\quad J_{17} = D_{11}^{(1)} + \frac{1}{\bar{R}_1}E_{11}^{(1)},\quad J_{18} = \frac{B_{12}^{(1)}}{\bar{R}_1} - K_s\left(A_{55}^{(1)} + \frac{1}{\bar{R}_1}B_{55}^{(1)}\right) + \frac{R_2G_{adh}h_1}{2\bar{R}_1}, \tag{A.4}$$

$$J_{19} = \frac{R_2G_{adh}h_1}{2\bar{R}_1}\left(\frac{d\eta_1(r)}{dr} - \frac{\eta_1(r)}{r}\right)_{r=R_2},\quad J_{20} = \frac{R_2G_{adh}h_1^2}{4\bar{R}_1}\left(\frac{d\eta_1(r)}{dr} - \frac{\eta_1(r)}{r}\right)_{r=R_2} - K_s\left(A_{55}^{(1)} + \frac{1}{\bar{R}_1}B_{55}^{(1)}\right),\quad J_{21} = \frac{R_2G_{adh}h_1}{2\bar{R}_1}\left(\frac{d\eta_2(r)}{dr} - \frac{\eta_2(r)}{r}\right)_{r=R_2}, \tag{A.5}$$

$$J_{22} = -\frac{R_2G_{adh}h_1h_2}{4\bar{R}_1}\left(\frac{d\eta_2(r)}{dr} - \frac{\eta_2(r)}{r}\right)_{r=R_2},\quad J_{23} = \frac{R_2G_{adh}h_1}{2\bar{R}_1}\left(\frac{d\eta_0(r)}{dr} - \frac{\eta_0(r)}{r}\right)_{r=R_2},\quad J_{24} = D_{11}^{(2)} + \frac{1}{\bar{R}_2}E_{11}^{(2)},\quad J_{25} = \frac{B_{12}^{(2)}}{\bar{R}_2} - K_s\left(A_{55}^{(2)} + \frac{1}{\bar{R}_2}B_{55}^{(2)}\right) + \frac{R_3G_{adh}h_2}{2\bar{R}_2}, \tag{A.6}$$

$$J_{26} = \frac{R_3G_{adh}h_2}{2\bar{R}_2}\left(\frac{d\eta_1(r)}{dr} - \frac{\eta_1(r)}{r}\right)_{r=R_3},\quad J_{27} = \frac{R_3G_{adh}h_1h_2}{4\bar{R}_2}\left(\frac{d\eta_1(r)}{dr} - \frac{\eta_1(r)}{r}\right)_{r=R_3},\quad J_{28} = \frac{R_3G_{adh}h_2}{2\bar{R}_2}\left(\frac{d\eta_2(r)}{dr} - \frac{\eta_2(r)}{r}\right)_{r=R_3},\quad J_{29} = -\frac{R_3G_{adh}h_2^2}{4\bar{R}_2}\left(\frac{d\eta_2(r)}{dr} - \frac{\eta_2(r)}{r}\right)_{r=R_3}, \tag{A.7}$$

$$J_{30}=\frac{R_3 G_{adh} h_2}{2\bar{R}_2}\left(\frac{d\eta_0(r)}{dr}-\frac{\eta_0(r)}{r}\right)_{r=R_3},\quad J_{31}=-\frac{A_{12}^{(1)}}{\bar{R}_1},\quad J_{32}=K_s\left(A_{55}^{(1)}+\frac{1}{\bar{R}_2}B_{55}^{(1)}\right)-\frac{B_{12}^{(1)}}{\bar{R}_1},\quad J_{33}=K_s\left(A_{55}^{(1)}+\frac{1}{\bar{R}_2}B_{55}^{(1)}\right),\quad J_{34}=\frac{F_{22}^{(1)}}{\bar{R}_1}-\frac{R_2 E_{adh}}{\bar{R}_1\left(R_3-R_2\right)}, \tag{A.8}$$

$$J_{35}=\frac{R_2 E_{adh}}{\bar{R}_1\left(R_3-R_2\right)},\quad J_{36}=-\frac{A_{12}^{(2)}}{\bar{R}_2},\quad J_{37}=K_s\left(A_{55}^{(2)}+\frac{1}{\bar{R}_2}B_{55}^{(2)}\right)-\frac{B_{12}^{(2)}}{\bar{R}_2},\quad J_{38}=K_s\left(A_{55}^{(2)}+\frac{1}{\bar{R}_2}B_{55}^{(2)}\right),\quad J_{39}=\frac{R_3 E_{adh}}{\bar{R}_2\left(R_3-R_2\right)},\quad J_{40}=-\frac{F_{22}^{(2)}}{\bar{R}_2}-\frac{R_3 E_{adh}}{\bar{R}_2\left(R_3-R_2\right)}, \tag{A.9}$$

$$J_{41}=2\pi\bar{R}_1\left(A_{11}^{(1)}+\frac{1}{\bar{R}_1}B_{11}^{(1)}\right)+K_2,\quad J_{42}=2\pi\bar{R}_1\left(B_{11}^{(1)}+\frac{1}{\bar{R}_1}D_{11}^{(1)}\right)+K_2\frac{h_1}{2},\quad J_{43}=2\pi A_{12}^{(1)},\quad J_{44}=2\pi\bar{R}_2\left(A_{11}^{(2)}+\frac{1}{\bar{R}_2}B_{11}^{(2)}\right)+K_3,\quad J_{45}=2\pi\bar{R}_2\left(A_{11}^{(2)}+\frac{1}{\bar{R}_2}B_{11}^{(2)}\right)-K_3\frac{h_2}{2} \tag{A.10}$$

$$J_{46}=2\pi A_{12}^{(2)},\quad J_{47}=K_1,\quad J_{48}=\frac{A_{12}^{(1)}}{\bar{R}_1},\quad J_{49}=\frac{A_{12}^{(2)}}{\bar{R}_2},\quad J_{50}=\frac{B_{12}^{(1)}}{\bar{R}_1}-K_s\left(A_{55}^{(1)}+\frac{1}{\bar{R}_1}B_{55}^{(1)}\right),\quad J_{51}=-K_s\left(A_{55}^{(1)}+\frac{1}{\bar{R}_1}B_{55}^{(1)}\right) \tag{A.11}$$

$$J_{52}=\frac{B_{12}^{(2)}}{\bar{R}_2}-K_s\left(A_{55}^{(2)}+\frac{1}{\bar{R}_2}B_{55}^{(2)}\right),\quad J_{53}=-K_s\left(A_{55}^{(2)}+\frac{1}{\bar{R}_2}B_{55}^{(2)}\right),\quad J_{54}=-\frac{A_{12}^{(1)}}{\bar{R}_1},\quad J_{55}=K_s\left(A_{55}^{(1)}+\frac{1}{\bar{R}_1}B_{55}^{(1)}\right)-\frac{B_{12}^{(1)}}{\bar{R}_1},\quad J_{56}=\frac{F_{22}^{(1)}}{\bar{R}_1}. \tag{A.12}$$

References

[1] Mittal, K.L., Panigrahi, S.K., (Eds.) *Structural Adhesive Joints: Design, Analysis and Testing*, Wiley-Scrivener, Beverly, MA, 2020.

[2] Shishesaz, M., *Stress distribution and design analysis of adhesively bonded tubular joints: A review*, Progress in Adhesion and Adhesives, Vol. 7, Mittal (Ed.), K.L., Chapter 1, Wiley-Scrivener, Beverly, MA, 2024.

[3] Shishesaz, M., Hosseini, M., Effects of joint geometry and material on stress distribution, strength and failure of bonded composite joints: an overview, *Journal of Adhesion*, 96, 2020, 1053-1121.

[4] Shishesaz, M., Reza, A., The effect of viscoelasticity of polymeric adhesives on shear stress distribution in a single-lap joint, *Journal of Adhesion*, 89, 2013, 859-880.

[5] Reza, A., Shishesaz, M., Naderantahan, K., The effect of viscoelasticity on creep behavior of double lap adhesively bonded joint, *Latin American Journal of Solids and Structures*, 11(1), 2014, 35-50.

[6] Goland, M., Reissner, E., The Stresses in Cemented joints, *Journal of Applied Mechanics, Transaction of ASME,* 11(1), 1944, A17-A27.

[7] Lubkin, J.L., Reissner, E., Stress distribution and design data for adhesive lap joints between circular tubes, *Journal of Applied Mechanics, Transaction of ASME*, 78, 1956, 1213-1221.

[8] Alwar, R.S., Nagaraja, Y.R., Viscoelastic analysis of an adhesive tubular joint, *Journal of Adhesion,* 8, 1976, 79-92.

[9] Adams, R.D., Peppiatt, N.A., Stress analysis of adhesive bonded tubular lap joints, *Journal of Adhesion*, 19, 1977, 1–18.

[10] Thomsen, O.T., Elasto-static and elasto-plastic stress analysis of adhesive bonded tubular lap joints, *Composite Structures,* 21, 1992, 249-259.

[11] Shi, Y.P., Cheng, S., Analysis of adhesive-bonded cylindrical lap joints subjected to axial load, *Journal of Engineering Mechanics,* 119, 1993, 584-602.

[12] Kim, Y.G., Lee, S.J., Lee, D.G., Jeong, K.S., Strength analysis of adhesively-bonded tubular single lap steel-steel joints under axial loads considering residual thermal stresses, *Journal of Adhesion,* 60, 1997, 125-140.

[13] Cho, D.H., Lee, D.G., Optimum design of co-cured steel–composite tubular single lap joints under axial load, *Journal of Adhesion Science and Technology*, 14(7), 2000, 939-63.

[14] Kim, J.K., Lee, D.G., Thermal characteristics of tubular single lap adhesive joints under axial loads, *Journal of Adhesion Science and Technology,* 15, 2001, 1511–1528.

[15] Vaziri, A., Nayeb-Hashemi, H., Dynamic response of tubular joints with an annular void subjected to a harmonic torsional load, *Proceedings of the Institution of Mechanical Engineers, Part K: Journal of Multi-body Dynamics*, 216(4), 2002, 361-70

[16] Pugno, N., Carpinteri, A., Tubular adhesive joints under axial load, *Journal of Applied Mechanics,* 70, 2003, 832-839.

[17] Nemes, O., Lachaud, F., Mojtabi, A., Contribution to the study of cylindrical adhesive joining, *International Journal of Adhesion and Adhesives*, 26, 2006, 474-480.

[18] Lees, J.M., Behaviour of GFRP adhesive pipe joints subjected to pressure and axial loadings, *Composites Part A: Applied Science and Manufacturing*, 37(8), 2006, 1171-1179.

[19] Kumar, S., Analysis of tubular adhesive joints with a functionally modulus graded bondline subjected to axial loads, *International Journal of Adhesion and Adhesives,* 29, 2009, 785-795.

[20] Das, R.R., Pradhan, B., Adhesion failure analyses of bonded tubular single lap joints in laminated fibre reinforced plastic composites, *International Journal of Adhesion and Adhesives*, 30, 2010, 425–438.

[21] Labbe, S., Drouet, J.-M., A multi-objective optimization procedure for bonded tubular-lap joints subjected to axial loading, *International Journal of Adhesion and Adhesives*, 33, 2012, 26–35.

[22] Dragoni, E., Goglio, L., Adhesive stresses in axially-loaded tubular bonded joints—Part I: Critical review and finite element assessment of published models, *International Journal of Adhesion and Adhesives,* 47, 2013, 35–45.

[23] Goglio, L., Paolino, D.S., Adhesive stresses in axially-loaded tubular bonded joints—Part II: Development of an explicit closed-form solution for the Lubkin and Reissner model, *International Journal of Adhesion and Adhesives,* 48, 2014, 35–42.

[24] Aimmanee, S., Hongpimolmas, P., Ruangjirakit, K., Simplified analytical model for adhesive-bonded tubular joints with isotropic and composite adherends subjected to tension, *International Journal of Adhesion and Adhesives,* 86, 2018, 59-72.

[25] Barbosa, D.R., Campilho, R.D.S.G., Rocha, R.J.B., Ferreira, L.R.F., Experimental and numerical assessment of tensile loaded tubular adhesive joints, *Journal of Materials: Design and Applications,* 233, 2019, 452–464.

[26] Shishesaz, M., Tehrani, S., The effects of circumferential voids or debonds on stress distribution in tubular adhesive joints under torsion, *Journal of Adhesion*, 96, 2019, 1396-1430.

[27] Shishesaz, M., Tehrani, S., Interfacial shear stress distribution in the adhesively bonded tubular joints under tension with a circumferential void or debond, *Journal of Adhesion Science and Technology,* 34, 2020, 1172-1205.

[28] Shishesaz, M., Bavi, N., Shear stress distribution in adhesive layers of a double-lap joint with void or bond separation, *Journal of Adhesion Science and Technology*, 27(11), 2013, 1197-225.

[29] Oh, J.H., Nonlinear analysis of adhesively bonded tubular single-lap joints for composites in torsion, *Composites Science and Technology*, 67, 2007, 1320–1329.

[30] daSilva, L.F.M., João, M., Lopes, C.Q., Joint strength optimization by the mixed-adhesive technique, *International Journal of Adhesion and Adhesives*, 29, 2009, 509–514.
[31] Shishesaz, M., Ghamarian, A., Moradi, S., Stress distribution in laminated composite tubular joints with damaged adhesive layer under torsion, *Journal of Adhesion*, 99, 2023, 930-971.
[32] Ghamarian, M., *Stress analysis of adhesively bonded laminated composite pipes with a tubular void or debond*, M.Sc. Thesis, Shahid Chamran University of Ahvaz, Ahvaz, Iran, 2021.

ORCID iD

Mohammad Shishesaz https://orcid.org/0000-0002-1892-1946
Reza Mosalmani https://orcid.org/0000-0002-8036-9638

How to cite this article: Shishesaz M., Ghamarian A.H., Mosalmani R. The Effects of Defects and Adherend Material on Adhesive Stress Distribution in Laminated Composite Tubular Joints Under Axial Tensile Loads, *J. Appl. Comput. Mech.*, 11(4), 2025, 1112-1138. https://doi.org/10.22055/jacm.2025.47828.4795